THE THREE DIMENSIONAL NEUMANN GREEN'S FUNCTION FOR GENERAL SURFACES: SINGULAR ASYMPTOTICS AND BOUNDARY INTEGRAL METHODS

ALAN E. LINDSAY *, ANDREW J. BERNOFF †, TRISTAN GOODWILL ‡, AND JEREMY G. HOSKINS §

Abstract. We present an asymptotic analysis and high-order boundary integral method for the three-dimensional Neumann Green's function in general geometries. The Neumann Green's function is a fundamental quantity which arises in numerous fields of science and engineering. In the application of singular perturbation methods to strongly localized reactions and diffusive transport, the Green's function plays the key role in mediating global dynamics. However, this essential quantity can only be determined in closed form for a limited set of geometries. The Green's function for the Laplacian is an elliptic problem with a Dirac forcing term. Accurate resolution of the solution requires a careful decomposition into a singular and a regular part. The bulk scenario is where the source is placed off surface and the singularity is given by the free-space function. In the surface case, where the source is placed at a curved point on the boundary, we use asymptotic analysis to determine a three-term singularity structure. With explicit knowledge of these singularities, we develop a high-order boundary integral method for the determination of the remaining regular part. To resolve the singular boundary data, our integral method uses a custom discretization with Duffy patches near the source. We validate our method using several test cases in which closed form solutions can be developed, including spheres, prolate spheroids and constructed domains. We demonstrate the applicability of our method to address some open problems in narrow capture theory.

Key words. Green's functions; Singular perturbation methods; Integral Methods; Narrow capture problems.

1. Introduction. The Neumann Green's function for the Laplacian (or Neumann function) is a fundamental quantity with applications across science and engineering, with examples ranging from electrostatics, acoustics, optics and diffusive processes [55, 17, 54, 49, 42, 50, 15, 8, 26, 21, 3]. For a closed geometry $\Omega \subset \mathbb{R}^3$ with boundary $\partial\Omega$, and a source point $\mathbf{x}_0$, the problem for the Neumann function can be posed either interior or exterior to Ω, with a bulk source ($\mathbf{x}_0 \notin \partial\Omega$) or a surface source ($\mathbf{x}_0 \in \partial\Omega$). These choices generate four related but distinct functions that have different normalization and singularity considerations. Our presentation will largely focus on the surface case which presents the most significant challenge.

In the case of a surface source $\mathbf{x}_0 \in \partial\Omega$, the exterior Neumann function $G^e(\mathbf{x};\mathbf{x}_0)$ for the Laplacian satisfies the boundary value problem

$$\Delta G^e = 0 \quad \text{in } \mathbb{R}^3 \setminus \Omega, \qquad \partial_n G^e = -\delta(\mathbf{x}-\mathbf{x}_0) \quad \text{on } \partial\Omega. \tag{1.1a}$$

The formulation (1.1) assumes that the Dirac distribution is two-dimensional in the surface coordinates. The choice of the negative sign implies a unit flux into the surface and imposes the far field solvability condition

$$G^e(\mathbf{x};\mathbf{x}_0) \sim \frac{1}{4\pi|\mathbf{x}|} \qquad \text{as} \qquad |\mathbf{x}| \to \infty. \tag{1.1b}$$

The *interior* surface Neumann function satisfies

$$\Delta G^i = \frac{1}{|\Omega|} \quad \text{in} \quad \Omega; \qquad \partial_n G^i = -\delta(\mathbf{x}-\mathbf{x}_0) \quad \text{on } \partial\Omega. \tag{1.2a}$$

The solution is unique up to a constant translation which can be fixed by the condition

$$\int_\Omega G^i(\mathbf{x};\mathbf{x}_0)\mathrm{d}V(\mathbf{x}) = 0. \tag{1.2b}$$

In the above formulations $\partial_n \equiv \hat{\mathbf{n}}\cdot\nabla$ is the normal derivative to $\partial\Omega$, with $\hat{\mathbf{n}}$ the outward pointing normal. The presence of the Dirac forcing term means that the Neumann function is singular as $\mathbf{x} \to \mathbf{x}_0$. A key step in resolving the Neumann function is to determine the correct singularity structure and establish the decomposition

$$G^{i,e}(\mathbf{x};\mathbf{x}_0) = G^{i,e}_{\text{sing}}(\mathbf{x};\mathbf{x}_0) + R^{i,e}(\mathbf{x};\mathbf{x}_0). \tag{1.3}$$

*University of Notre Dame, Notre Dame, IN, 46556, USA. Email: a.lindsay@nd.edu (corresponding author),
†Harvey Mudd College, Claremont, CA, USA Email: andrew.bernoff@gmail.com
‡Department of Statistics, University of Chicago, USA. Email: tgoodwill@uchicago.edu
§Department of Statistics, University of Chicago, USA and NSF-Simons National Institute for Theory and Mathematics in Biology, Chicago, IL. Email: jeremyhoskins@uchicago.edu

In the formulation (1.3) $G^{i,e}_{\text{sing}}(\mathbf{x};\mathbf{x}_0)$ is singular as $\mathbf{x}\to\mathbf{x}_0$ and $R^{i,e}(\mathbf{x};\mathbf{x}_0)$ is bounded as $\mathbf{x}\to\mathbf{x}_0$. In our treatment of these problems, both asymptotically and numerically, we will largely be focused on the more delicate surface case. In the simpler *bulk* case ($\mathbf{x}_0\notin\partial\Omega$),

$$G^{i,e}_{\text{sing}}(\mathbf{x};\mathbf{x}_0) = G_F(\mathbf{x}-\mathbf{x}_0), \qquad G_F(\mathbf{x}) = \frac{1}{4\pi|\mathbf{x}|}. \tag{1.4}$$

which is the standard free space Green's function for the Laplacian in three dimensions. The surface case ($\mathbf{x}_0\in\partial\Omega$) dramatically alters the nature of the singular solution behavior. The precise behavior of the singular component $G^{i,e}_{\text{sing}}(\mathbf{x};\mathbf{x}_0)$ for $\mathbf{x}_0\in\partial\Omega$ has been the topic of several studies due its centrality in the asymptotic solution of the narrow escape problem describing the escape rate of Brownian particles through a small boundary windows [15, 50, 37, 13, 26, 6] and in superconductivity [42, 49]. The recent study of [43] used a pseudodifferential operator approach to identify a triple singularity structure featuring a monopole term twice the strength of the free-space term (1.4), a logarithmic singularity with strength proportional to the mean curvature at $\mathbf{x}_0$ and a weaker singularity that depends on the difference of principal curvatures at $\mathbf{x}_0$.

Singularity structure of the Green's function. We provide here a derivation of the singular behavior $G^{i,e}_{\text{sing}}(\mathbf{x};\mathbf{x}_0)$ as $\mathbf{x}\to\mathbf{x}_0$ for $\mathbf{x}_0\in\partial\Omega$ using a local expansion of the Laplacian in tangent plane coordinates near $\mathbf{x}_0$. Our analysis re-derives the result obtained in [43], but with a formulation that is adaptable to boundary integral equation methods for accurate evaluation of $R^{i,e}(\mathbf{x};\mathbf{x}_0)$. The result takes the form

$$G^{i,e}_{\text{sing}}(\mathbf{x};\mathbf{x}_0) \sim \frac{1}{2\pi|\mathbf{x}-\mathbf{x}_0|} \mp \frac{\mathcal{H}(\mathbf{x}_0)}{4\pi}\log\big[\,|\mathbf{x}-\mathbf{x}_0|+\eta\,\big] \pm \mathcal{Q}(\mathbf{x}_0)\,e(\mathbf{x};\mathbf{x}_0), \quad \text{as} \quad \mathbf{x}\to\mathbf{x}_0, \tag{1.5a}$$

where $\eta = (\mathbf{x}-\mathbf{x}_0)\cdot\hat{\mathbf{n}}$ is the distance from $\mathbf{x}\in\Omega$ to the tangent plane at $\mathbf{x}_0\in\partial\Omega$. The upper and lower signs reflect the exterior and interior singularities respectively. The local geometric quantities are defined as

$$\mathcal{H}(\mathbf{x}_0) = \frac{\kappa_1(\mathbf{x}_0)+\kappa_2(\mathbf{x}_0)}{2}, \qquad \mathcal{Q}(\mathbf{x}_0) = \frac{\kappa_1(\mathbf{x}_0)-\kappa_2(\mathbf{x}_0)}{2}, \tag{1.5b}$$

where $\kappa_j(\mathbf{x}_0)$ for $j=1,2$ denote the principal curvatures of the surface at $\mathbf{x}_0$. The quantity $\mathcal{H}(\mathbf{x}_0)$ is the mean curvature at $\mathbf{x}_0\in\partial\Omega$ while $\mathcal{Q}(\mathbf{x}_0)$ is a measure of the anisotropy in the surface curvature. The function $e(\mathbf{x};\mathbf{x}_0)$ is a weaker singularity that remains finite in Ω near $\mathbf{x}_0$ but has a different limiting value depending on the direction that $\mathbf{x}$ approaches $\mathbf{x}_0$, analogous to the behavior of $(x^2-y^2)/(x^2+y^2)$ as $(x,y)\to(0,0)$. In (2.16), we derive the explicit limiting behavior

$$e(\mathbf{x};\mathbf{x}_0) \sim \frac{1}{8\pi}\left[\frac{|\mathbf{x}-\mathbf{x}_0|-\eta}{|\mathbf{x}-\mathbf{x}_0|+\eta}\right]\cos(2\varphi), \quad \text{as} \quad \mathbf{x}\to\mathbf{x}_0.$$

Here φ is an azimuthal measure in the tangent plane to $\partial\Omega$ at $\mathbf{x}_0\in\partial\Omega$ (see Fig. 2.1).

The main challenge addressed in this work is to reliably compute the solution of the regular part $R^{i,e}(\mathbf{x};\mathbf{x}_0)$ while precisely implementing the surface singularity behavior (1.5) and the normalization conditions (1.1b) and (1.2b). The Green's functions solving (1.1) and (1.2) have so far only been accessible for simple geometries such as the sphere [42, 15, 14], prolate and oblate spheroids [55] and ellipsoids [17]. Moreover, these solutions take the form of slowly convergent expansions in associated Legendre functions or Lamé functions whose reliable numerical evaluation has many associated issues [54]. However, for many important applications, it is essential to determine this function for general curved surfaces [49, 50, 24, 32]. In chemotaxis and chemical signaling, an open problem of broad interest is to understand the role that curvature plays in biological signaling processes involving diffusion [1, 47, 45, 35]. Matched asymptotic analysis is a powerful tool for approximating the solution of cell signaling problems in non-radially symmetric geometries, however, it expresses these solutions in terms of global quantities related to the Neumann function [4, 37, 14, 26, 51].

A recent review article [13] raised the lack of reliable computation of the Neumann function as an obstacle for the application of matched asymptotic methods for capture problems. The contribution of this work is to fill this gap by providing a high-order boundary integral method that can evaluate solutions of (1.1-1.2) for general three-dimensional geometries. Our method exactly captures the singularity behavior (1.5) for

both the bulk ($\mathbf{x}_0 \notin \partial\Omega$) and surface ($\mathbf{x}_0 \in \partial\Omega$) cases while resolving for the regular part $R^{i,e}(\mathbf{x};\mathbf{x}_0)$. For the interior Green's function, it exactly implements the global condition (1.2b).

The paper is structured as follows. In Section 2, we perform an asymptotic analysis in the vicinity of a source $\mathbf{x}_0 \in \partial\Omega$ located on a curved surface, leading to the singularity behavior (1.5). In Section 3 we describe our boundary integral method for the resolution of the regular part $R^{i,e}(\mathbf{x};\mathbf{x}_0)$ of the Green's function while exactly implementing the singularity behavior and integral constraints. In Section 4 we validate the accuracy of our methods on a range of known solutions for some simple geometries. We also demonstrate the applicability of the method to inform on the question of optimal arrangements of target sites in narrow capture problems. Finally in Section 5 we conclude with some avenues for future research and potential applications of this method.

2. Asymptotic analysis of the singular solution structure. In this section, we derive the singular structure of the surface Green's function in the vicinity of the source point $\mathbf{x}_0 \in \partial\Omega$. In our derivation, we use a coordinate system near the source that will later facilitate numerical solution. For clarity we will proceed by deriving the relevant behavior for the exterior case.

2.1. The tangent plane coordinate system. In this section we use an orthogonal coordinate system that is a rotated and translated version of $\mathbb{R}^3$. By orienting the coordinates along the principal axes at a point, we can reduce the number of terms in the local expansion of the surface. Consider a coordinate system centered at the source $\mathbf{x}_0$:

$$\mathbf{x} - \mathbf{x}_0 = \eta\,\hat{\mathbf{n}} + p_1\hat{\mathbf{t}}_1 + p_2\hat{\mathbf{t}}_2, \tag{2.1}$$

where $\hat{\mathbf{n}}$ is the outward pointing unit normal to $\partial\Omega$ at $\mathbf{x}_0$, and $\hat{\mathbf{t}}_1, \hat{\mathbf{t}}_2$ are perpendicular tangent vectors aligned to the principal curvatures, κ_1 and κ_2, which are taken as negative when Ω is convex (which is consistent with an outward pointing normal). The mean curvature, $\mathcal{H}$, and the curvature difference, $\mathcal{Q}$, at $\mathbf{x}_0$ are defined by (1.5b). The surface can be locally defined by a function

$$\eta = f(p_1, p_2) = \frac{\kappa_1 p_1^2 + \kappa_2 p_2^2}{2} + \mathcal{O}(p_1^3, p_2^3),$$

or implicitly as

$$\mathcal{S}(p_1, p_2, \eta) := \eta - f(p_1, p_2) = 0.$$

It is convenient to also define a local cylindrical version of these coordinates by

$$(p_1, p_2, \eta) = (r\cos\varphi, r\sin\varphi, \eta), \tag{2.2a}$$

where we have that

$$r = \sqrt{p_1^2 + p_2^2}, \qquad \eta = \hat{\mathbf{n}}\cdot(\mathbf{x} - \mathbf{x}_0), \qquad \rho \equiv |\mathbf{x} - \mathbf{x}_0| = \sqrt{\eta^2 + r^2}\,. \tag{2.2b}$$

A schematic of the local coordinate system on the tangent plane is shown in Fig. 2.1.

2.2. The leading order Green's function. Our aim is to write the Green's function in the form

$$G(\mathbf{x};\mathbf{x}_0) = G_{\text{sing}}(\mathbf{x};\mathbf{x}_0) + R(\mathbf{x};\mathbf{x}_0), \tag{2.3}$$

where $G_{\text{sing}}(\mathbf{x};\mathbf{x}_0)$ is the singular portion of the Green's function and $R(\mathbf{x};\mathbf{x}_0)$ is the regular part. When the source is placed in the bulk, the singularity corresponds to the free space function $G_{\text{sing}}(\mathbf{x};\mathbf{x}_0) = (4\pi|\mathbf{x} - \mathbf{x}_0|)^{-1}$. Our derivation will leave a regular part that satisfies the condition

$$\lim_{\mathbf{x}\to\mathbf{x}_0} |\hat{\mathbf{n}}\cdot\nabla R| = 0, \qquad \text{where} \qquad \mathbf{x} \in \partial\Omega,$$

which allows G_{sing} to be arbitrary up to a harmonic function whose normal derivative vanishes at $\mathbf{x}_0$. This will suffice to uniquely determine the Neumann problem for R. In order to calculate an expansion for non-flat geometries, we first note that the unit normal on $\mathcal{S}$ can be written as

$$\hat{\mathbf{n}}(p,q) = \frac{\nabla\mathcal{S}}{|\nabla\mathcal{S}|} = \frac{(-f_{p_1}, -f_{p_2}, 1)}{\sqrt{1 + (f_{p_1})^2 + (f_{p_2})^2}}\,,$$

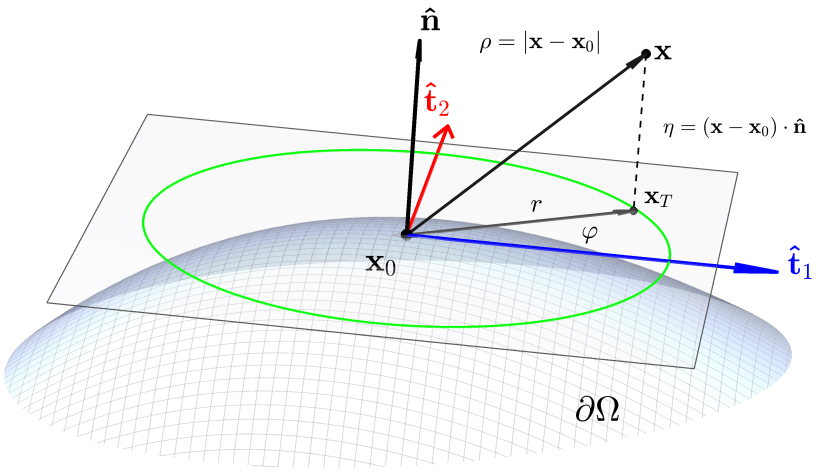

Fig. 2.1: Local coordinate system near the point $\mathbf{x}_0 \in \partial\Omega$ and exterior to $\partial\Omega$. The unit vectors $\hat{\mathbf{t}}_1$,$\hat{\mathbf{t}}_2$ (2.1) lay along the principal directions. The local cylindrical coordinates system (r, φ, η) is defined in (2.2).

which gives the following formula for $\partial_n G$ on $\partial\Omega$,

$$\partial_n G|_{\partial\Omega} = \hat{\mathbf{n}}(p_1, p_2) \cdot \nabla G|_{\partial\Omega} = \left. \frac{\partial_\eta G - f_{p_1}\partial_{p_1} G - f_{p_2}\partial_{p_2} G}{\sqrt{1 + (f_{p_1})^2 + (f_{p_2})^2}} \right|_{\mathcal{S}=0} .$$

The transformed Dirac source takes the form

$$\delta(\mathbf{x} - \mathbf{x}_0) = \sqrt{1 + (f_{p_1})^2 + (f_{p_2})^2}\, \delta(p_1)\delta(p_2),$$

where the multiplicative factor is the area element, $\mathrm{d}A = \sqrt{1 + (f_{p_1})^2 + (f_{p_2})^2}\, dp_1\, dp_2$. However, if we specify $f_{p_1}(0,0) = f_{p_2}(0,0) = 0$ then the area element at the source evaluates to unity. Consequently, we can reduce the boundary condition to

$$\partial_\eta G - f_{p_1}\partial_{p_1} G - f_{p_2}\partial_{p_2} G = -\delta(p_1)\delta(p_2) \qquad (p_1, p_2) \in \mathbb{R}^2, \tag{2.4}$$

which is valid in the region where the surface can be represented as a graph $\eta = f(p_1, p_2)$.

2.3. The local perturbation expansion. Guided by the leading order, we now rescale space in the neighborhood of the source,

$$(p_1, p_2, \eta) = (\varepsilon\mu, \varepsilon\nu, \varepsilon\zeta),$$

and also define associated cylindrical coordinates,

$$\mu = r\cos\varphi, \quad \nu = r\sin\varphi, \quad r = \sqrt{\mu^2 + \nu^2}, \quad \rho = \sqrt{r^2 + \zeta^2}.$$

On the surface,

$$\zeta = \frac{1}{\varepsilon} f(\varepsilon\mu, \varepsilon\nu) = \varepsilon \frac{\kappa_1\mu^2 + \kappa_2\nu^2}{2} + \mathcal{O}(\varepsilon^2).$$

Correspondingly, the boundary condition becomes

$$\frac{1}{\varepsilon}\left[\partial_\zeta G - f_{p_1}\partial_\mu G - f_{p_2}\partial_\nu G\right] = -\frac{1}{\varepsilon^2}\delta(\mu)\delta(\nu) \qquad (p_1, p_2) \in \mathbb{R}^2, \quad \zeta = f, \tag{2.5}$$

where

$$f_{p_1}(\varepsilon\mu, \varepsilon\nu) = \varepsilon\kappa_1\mu + \mathcal{O}(\varepsilon^2) \ , \quad f_{p_2}(\varepsilon\mu, \varepsilon\nu) = \varepsilon\kappa_2\nu + \mathcal{O}(\varepsilon^2) \ .$$

The Green's function is now expanded as

$$G(p_1, p_2, \eta) = \frac{1}{\varepsilon} g_0(\mu, \nu, \zeta) + g_1(\mu, \nu, \zeta) + \varepsilon g_2(\mu, \nu, \zeta) + \mathcal{O}(\varepsilon^2).$$

We now expand the equation and the boundary condition and collect terms at each order.

$\underline{\mathcal{O}(\varepsilon^{-2})}$: At leading order, we obtain the upper half-plane problem

$$\Delta g_0 = 0, \qquad \zeta > 0; \tag{2.6a}$$

$$\partial_\zeta g_0 = -\delta(\mu)\delta(\nu), \qquad \zeta = 0, \quad (\mu, \nu) \in \mathbb{R}^2 \ , \tag{2.6b}$$

where $\Delta \equiv \partial_\mu^2 + \partial_\nu^2 + \partial_\zeta^2$. The general solution is

$$g_0 = \frac{1}{2\pi\rho}, \tag{2.7}$$

defined up to an additive constant.

$\underline{\mathcal{O}(\varepsilon^{-1})}$: At this order, we expand the boundary condition noting that

$$\partial_\mu g_0 = -\frac{\mu}{2\pi\rho^3}, \qquad \partial_\nu g_0 = -\frac{\nu}{2\pi\rho^3}, \qquad \partial_\zeta g_0 = -\frac{\zeta}{2\pi\rho^3}.$$

Also, on the boundary $\rho(\mu, \nu, \zeta) = \rho(\mu, \nu, 0)[1 + \mathcal{O}(\varepsilon)] = r[1 + \mathcal{O}(\varepsilon)]$. This allows us to expand the Neumann boundary condition to obtain the correction problem

$$\Delta g_1 = 0, \qquad \zeta > 0; \tag{2.8a}$$

$$\partial_\zeta g_1 = -\frac{\kappa_1 \mu^2 + \kappa_2 \nu^2}{4\pi r^3}, \qquad \zeta = 0, \quad (\mu, \nu) \in \mathbb{R}^2 \tag{2.8b}$$

The boundary condition in cylindrical coordinates is

$$\partial_\zeta g_1 = -\frac{1}{4\pi r} \left[\mathcal{H} + \mathcal{Q} \cos(2\varphi)\right] \qquad \zeta = 0.$$

To solve (2.8), we seek a solution of form

$$g_1 = \Xi(r, \zeta) + \chi(r, \zeta) \cos(2\varphi).$$

Here the coefficient functions satisfy the problems

$$\begin{cases} \Xi_{\zeta\zeta} + \Xi_{rr} + \dfrac{1}{r}\Xi_r = 0, & r, \zeta > 0 \\ \Xi_\zeta = -\dfrac{\mathcal{H}}{4\pi r}, & \zeta = 0 \end{cases} \qquad \begin{cases} \chi_{\zeta\zeta} + \chi_{rr} + \dfrac{1}{r}\chi_r - \dfrac{4}{r^2}\chi = 0, & r, \zeta > 0 \\ \chi_\zeta = -\dfrac{\mathcal{Q}}{4\pi r}, & \zeta = 0. \end{cases} \tag{2.9a}$$

From an application of the Hankel transform, we find the solutions of these problems to be

$$\Xi(r, \zeta) = -\frac{\mathcal{H}}{4\pi} \log\left[\rho + \zeta\right], \qquad \chi(r, \zeta) = \frac{\mathcal{Q}}{8\pi} \left[\frac{\rho - \zeta}{\rho + \zeta}\right]. \tag{2.9b}$$

This yields the following expression for the monopole correction

$$g_1(\mu, \nu, \zeta) = -\frac{\mathcal{H}}{4\pi} \log\left[\rho + \zeta\right] + \frac{\mathcal{Q}}{8\pi} \left[\frac{\rho - \zeta}{\rho + \zeta}\right] \cos(2\varphi). \tag{2.10}$$

The second term in the expression (2.10) can be rewritten as

$$\left[\frac{\rho - \zeta}{\rho + \zeta}\right] \cos(2\varphi) = \left[\frac{\rho - \zeta}{\rho + \zeta}\right] \frac{\mu^2 - \nu^2}{r^2} = \frac{\mu^2 - \nu^2}{(\rho + \zeta)^2} \ ,$$

by using the relationship $\rho^2 = r^2 + \zeta^2$. For fixed positive ζ, we have the behavior

$$g_1(\mu,\nu,\zeta) \sim -\frac{\mathcal{H}}{4\pi}\log(2\zeta) + \left[-\frac{\mathcal{H}}{16\pi\zeta^2} + \frac{\mathcal{Q}}{32\pi\zeta^2}\cos(2\varphi)\right] r^2 + \mathcal{O}(r^4),$$

as $r \to 0$ which demonstrates that the solution is differentiable (even analytic) in this limit. However, we observe that the solution is singular at the origin; along rays from the origin the mean curvature term blows up like $\log\rho$ and depends on the polar angle while the curvature difference term depends on both the polar and azimuthal angle.

$\underline{\mathcal{O}(\varepsilon^0)}$: To better understand the error structure of the expansion, we proceed to the next order which requires a higher order expansion of the boundary. This is given by

$$f(p_1,p_2) = \frac{\kappa_1 p_1^2 + \kappa_2 p_2^2}{2} + \left(c_{30}p_1^3 + c_{21}p_1^2p_2 + c_{12}p_1p_2^2 + c_{03}p_2^3\right) + \mathcal{O}(r^4)\ . \tag{2.11}$$

The high order correction $g_2(\mu,\nu,\zeta)$ satisfies

$$\Delta g_2 = 0 \qquad \zeta > 0 \tag{2.12a}$$

$$\begin{aligned}\partial_\zeta g_2 = &-\left[\frac{\mathcal{H}^2}{4\pi} + \mathcal{Q}\mathcal{H}\frac{\mu^4-\nu^4}{2\pi r^4} + \mathcal{Q}^2\frac{\mu^4 - 6\mu^2\nu^2+\nu^4}{4\pi r^4}\right]\\ &-\left[\frac{c_{30}\mu^3 + c_{21}\mu^2\nu + c_{12}\mu\nu^2 + c_{03}\nu^3}{\pi r^3}\right] \qquad \zeta = 0, \quad (\mu,\nu)\in\mathbb{R}^2\ ,\end{aligned} \tag{2.12b}$$

The boundary condition can be rewritten in cylindrical coordinates as

$$\Delta g_2 = 0, \qquad \zeta > 0; \tag{2.13a}$$

$$\begin{aligned}\partial_\zeta g_2 = &-\left[\frac{\mathcal{H}^2}{4\pi} + \frac{\mathcal{Q}\mathcal{H}}{2\pi}\cos(2\varphi) + \frac{\mathcal{Q}^2}{4\pi}\cos(4\varphi)\right] \qquad \zeta = 0, \quad (\mu,\nu)\in\mathbb{R}^2.\\ &-\left[\frac{c_{12}+3c_{30}}{4\pi}\cos(\varphi) + \frac{c_{21}+3c_{03}}{4\pi}\sin(\varphi) + \frac{c_{30}-c_{12}}{4\pi}\cos(3\varphi) + \frac{c_{03}-c_{21}}{4\pi}\sin(3\varphi)\right]\ ,\end{aligned} \tag{2.13b}$$

together with appropriate decay conditions in the far-field. By linearity, g_2 will be a sum of terms of form

$$g_2^c(\zeta,r,\varphi) = \Phi_n(\zeta,r)\cos(n\varphi), \qquad g_2^s(\zeta,r,\phi) = \Phi_n(\zeta,r)\sin(n\varphi),$$

where $\Phi_n(\zeta,r)$ satisfies

$$\Phi_{n,\zeta\zeta} + \Phi_{n,rr} + \frac{1}{r}\Phi_{n,r} - \frac{n^2}{r^2}\Phi = 0 \qquad \zeta > 0; \tag{2.14a}$$

$$\Phi_{n,\zeta} = 1 \qquad \zeta = 0\ . \tag{2.14b}$$

For $n = 0$ we find that

$$\Phi_0(\zeta,r) = \zeta\ ,$$

and using Green's function and similarity methods, we find that

$$\Phi_1(\zeta,r) = \frac{r}{2}\log(\rho+\zeta) + \frac{\zeta(\rho-\zeta)}{2r}\ , \qquad \Phi_2(\zeta,r) = -\frac{1}{3}\frac{(2\rho+\zeta)(\rho-\zeta)^2}{r^2}, \tag{2.15a}$$

$$\Phi_3(\zeta,r) = -\frac{1}{8}\frac{(3\rho+\zeta)(\rho-\zeta)^3}{r^3}, \qquad \Phi_4(\zeta,r) = -\frac{1}{15}\frac{(4\rho+\zeta)(\rho-\zeta)^4}{r^4}\ , \tag{2.15b}$$

where $\rho = \sqrt{r^2+\zeta^2}$. We note that Φ_0 vanishes on the tangent plane, $\Phi_1 \sim r\log r$, and $\Phi_n \sim r$ for $n = 2,3,4$ which means that g_2 does not contribute to the regular part at $\mathbf{x}_0$.

2.4. Reconstituting the Green's function and the regular part. At this point, we bring together the final expression for the singular part of the Green's function, G_{sing}. In terms of the coordinates $(p_1, p_2, \eta) = (\varepsilon\mu, \varepsilon\nu, \varepsilon\zeta)$, we have that

$$\begin{aligned}\frac{1}{\varepsilon} g_0(\mu,\nu,\zeta) &= g_0(p_1,p_2,\eta)\ ,\\ g_1(\mu,\nu,\zeta) &= g_1(p_1,p_2,\eta) + \frac{\mathcal{H}}{4\pi}\log\varepsilon\ ,\\ \varepsilon g_2(\mu,\nu,\zeta) &= g_2(p_1,p_2,\eta) + [C_1 p_1 + C_2 p_2]\log\varepsilon,\end{aligned}$$

for appropriate constants C_1 and C_2. This allows us to identify

$$G_{\text{sing}}(p_1,p_2,\eta) \sim g_0(p_1,p_2,\eta) + g_1(p_1,p_2,\eta) + g_2(p_1,p_2,\eta) \sim g_0(p_1,p_2,\eta) + g_1(p_1,p_2,\eta) + \mathcal{O}(r\log r,\eta).$$

Recalling the definition $\eta = (\mathbf{x}-\mathbf{x}_0)\cdot\hat{\mathbf{n}}$, we arrive at the form of the singularity behavior

$$\begin{aligned}G_{\text{sing}}(p_1,p_2,\eta) &= g_0(p_1,p_2,\eta) + g_1(p_1,p_2,\eta)\\ &= \frac{1}{2\pi|\mathbf{x}-\mathbf{x}_0|} - \frac{\mathcal{H}}{4\pi}\log\left[|\mathbf{x}-\mathbf{x}_0|+\eta\right] + \frac{\mathcal{Q}}{8\pi}\left[\frac{|\mathbf{x}-\mathbf{x}_0|-\eta}{|\mathbf{x}-\mathbf{x}_0|+\eta}\right]\cos(2\varphi).\end{aligned} \tag{2.16}$$

Now that the singular piece of the Green's function has been isolated, we decompose into

$$G(\mathbf{x};\mathbf{x}_0) = G_{\text{sing}}(p_1,p_2,\eta) + R(\mathbf{x};\mathbf{x}_0).$$

In the case of the exterior problem, the regular part $R(\mathbf{x};\mathbf{x}_0)$ satisfies the Neumann problem

$$\Delta R = 0 \quad \text{in} \quad \mathbb{R}^3\setminus\Omega, \qquad \partial_n R|_{\partial\Omega} = \begin{cases} -\partial_n G_{\text{sing}}, & \mathbf{x}\neq\mathbf{x}_0;\\ 0, & \mathbf{x}=\mathbf{x}_0.\end{cases} \tag{2.17}$$

We note that $\partial_n R|_{\partial\Omega}$ is bounded but (as can be seen from the boundary condition (2.13b) for g_2 above) depends on the angle φ from which the singularity is approached as $\mathbf{x}\to\mathbf{x}_0$. The numerical treatment of this milder singularity is described in section 3.3.6.

The interior problem is similar but with the forcing term $1/|\Omega|$ in the right hand side of (2.17). This source term contributes only to the regular part of the solution leaving a singularity structure that is similar to the exterior problem, but with sign changes in the coefficients of the curvature dependent terms.

3. Boundary integral solution of the regular part of the Green's function. In order to obtain accurate solutions of (1.1) and (1.2) which effectively capture the singularities in the Neumann Green's function as $\mathbf{x}\to\mathbf{x}_0$, we first perform a standard reduction of the problem to a boundary integral equation (BIE) [34] for an unknown density σ on the boundary. A point of departure from existing BIE methods is the singular nature of the boundary data, which requires a custom discretization of the portion of the geometry in the vicinity of the source, and careful evaluation of the right hand side in order to mitigate effects of catastrophic cancellations and retain high-order convergence. In this section, we outline our approach. We begin by introducing several auxiliary functions and their analytic properties which are useful in the construction of suitable boundary data for our integral equations. Following this, we review the reduction of (1.1) and (1.2) to BIEs and the classical approach for enforcing integral constraints in the interior problem. Finally, we sketch a common approach to discretize BIEs and detail the modifications required to treat our boundary data.

3.1. Analytic properties of the corrections. Consider the functions ϕ, ψ defined by

$$\phi(\mu,\nu,\eta) = \log(\rho+\eta), \qquad \psi(\mu,\nu,\eta) = \frac{(\mu^2-\nu^2)}{(\rho+\eta)^2}, \tag{3.1}$$

with $\rho = \sqrt{\mu^2+\nu^2+\eta^2}$. A direct calculation shows that ϕ and ψ are harmonic away from the half-line $\{(0,0,\eta)\,|\,\eta\le 0\}$. In this section we describe modifications of the functions ϕ and ψ which have the same behavior near the origin, but have singularities lying only on a finite line segment. The key observation is given in the following lemma.

LEMMA 3.1. *Given ϕ and ψ as defined above, for any (μ,ν,η) not on the ray $\{(0,0,\eta)\,|\,\eta\le 0\}$, we have*

$$\frac{\partial}{\partial\eta}\phi(\mu,\nu,\eta)=\frac{1}{\rho},\qquad \frac{\partial^3}{\partial\eta^3}\psi(\mu,\nu,\eta)=-2\left(\frac{\partial^2}{\partial\mu^2}\frac{1}{\rho}-\frac{\partial^2}{\partial\nu^2}\frac{1}{\rho}\right).$$

The proof is straightforward, and omitted. Applying the fundamental theorem of calculus immediately gives the following corollary.

COROLLARY 3.2. *For any $\eta_2<0$ and any (μ,ν,η) not on the ray $\{(0,0,\eta)\,|\,\eta\le 0\}$,*

$$\phi(\mu,\nu,\eta)-\phi(\mu,\nu,\eta-\eta_2)=-\int_{\eta_2}^{0}\frac{1}{\sqrt{\mu^2+\nu^2+(\eta-t)^2}}\,\mathrm{d}t, \tag{3.2}$$

and

$$\begin{aligned}\psi(\mu,\nu,\eta)-\psi(\mu,\nu,\eta-\eta_2)+\eta_2\psi'(\mu,\nu,\eta-\eta_2)-\frac{\eta_2^2}{2}\psi''(\mu,\nu,\eta-\eta_2)\\ =2\int_{\eta_2}^{0}\int_{\eta_2}^{t}\int_{\eta_2}^{s}\left(\frac{\partial^2}{\partial\mu^2}\frac{1}{\sqrt{\mu^2+\nu^2+(\eta-u)^2}}-\frac{\partial^2}{\partial\nu^2}\frac{1}{\sqrt{\mu^2+\nu^2+(\eta-u)^2}}\right)\mathrm{d}u\,\mathrm{d}s\,\mathrm{d}t,\end{aligned} \tag{3.3}$$

with $\psi'(\mu,\nu,\eta)=\frac{\partial}{\partial\eta}\psi(\mu,\nu,\eta)$ and $\psi''(\mu,\nu,\eta)=\frac{\partial^2}{\partial\eta^2}\psi(\mu,\nu,\eta)$.

By interchanging the order of derivatives and integration, it is easily seen that the right-hand sides of (3.2) and (3.3) are harmonic away from the line segment $\{(0,0,\eta)\,|\,\eta_2\le\eta\le 0\}$ and are $O(1/\rho)$ and $O(1/\rho^3)$, respectively, as $\rho\to\infty$ uniformly in angle. It follows that the left-hand sides of the corresponding equations have removable singularities on the ray $\{(0,0,\eta)\,|\,\eta<\eta_2\}$.

The following corollary, which amounts to a change of the order of integration in (3.3), gives a more convenient expression for the integral in (3.3).

COROLLARY 3.3. *Let ψ and η_2 be as above. Then*

$$\begin{aligned}\psi(\mu,\nu,\eta)-\psi(\mu,\nu,\eta-\eta_2)+\eta_2\psi'(\mu,\nu,\eta-\eta_2)-\frac{\eta_2^2}{2}\psi''(\mu,\nu,\eta-\eta_2)\\ =\int_{\eta_2}^{0}t^2\left(\frac{\partial^2}{\partial\mu^2}\frac{1}{\sqrt{\mu^2+\nu^2+(\eta-t)^2}}-\frac{\partial^2}{\partial\nu^2}\frac{1}{\sqrt{\mu^2+\nu^2+(\eta-t)^2}}\right)\mathrm{d}t.\end{aligned} \tag{3.4}$$

Finally, the following lemma establishes properties of a related function that will be convenient in numerical simulations.

LEMMA 3.4. *For any $\eta_2<\eta_1<\eta_0<0$, if*

$$c_0=-\frac{\eta_1\eta_2}{(\eta_1-\eta_0)(\eta_0-\eta_2)},\qquad c_1=-\frac{\eta_0\eta_2}{(\eta_0-\eta_1)(\eta_1-\eta_2)},\qquad c_2=-\frac{\eta_0\eta_1}{(\eta_0-\eta_2)(\eta_2-\eta_1)},$$

set

$$\psi_{\eta_0,\eta_1,\eta_2}(\mu,\nu,\eta)=\psi(\mu,\nu,\eta)-c_0\psi(\mu,\nu,\eta-\eta_0)-c_1\psi(\mu,\nu,\eta-\eta_1)-c_2\psi(\mu,\nu,\eta-\eta_2).$$

Then $\psi_{\eta_0,\eta_1,\eta_2}$ is harmonic, except on $\{(0,0,\eta)\,|\,\eta_2\le\eta\le 0\}$, and is $O(1/\rho^3)$ uniformly in angle as $\rho\to\infty$.

Proof. Using Corollary 3.3 we observe that for $\psi_j(\mu,\nu,\eta):=\psi(\mu,\nu,\eta-\eta_j)$, then

$$\psi_j(\mu,\nu,\eta)=\psi(\mu,\nu,\eta-\eta_2)-(\eta_2-\eta_j)\psi'(\mu,\nu,\eta-\eta_2)+\frac{(\eta_2-\eta_j)^2}{2}\psi''(\mu,\nu,\eta-\eta_2)+I_j,$$

where

$$I_j=\int_{\eta_2}^{\eta_j}(t-\eta_j)^2\left(\frac{\partial^2}{\partial\mu^2}\frac{1}{\sqrt{\mu^2+\nu^2+(\eta-t)^2}}-\frac{\partial^2}{\partial\nu^2}\frac{1}{\sqrt{\mu^2+\nu^2+(\eta-t)^2}}\right)\mathrm{d}t,$$

for $j=0,1,2$. It is easily seen that the coefficients c_0,c_1,c_2 satisfy $\sum_{j=0}^{2}\eta_j^k c_j=\delta_{k,0}$, with $k=0,1,2$. It follows that

$$\psi_{\eta_0,\eta_1,\eta_2}(\mu,\nu,\eta)=I-c_0I_0-c_1I_1,$$

with

$$I = \int_{\eta_2}^{0} t^2 \left(\frac{\partial^2}{\partial \mu^2} \frac{1}{\sqrt{\mu^2+\nu^2+(\eta-t)^2}} - \frac{\partial^2}{\partial \nu^2} \frac{1}{\sqrt{\mu^2+\nu^2+(\eta-t)^2}} \right) \mathrm{d}t.$$

The rest of the proof follows immediately from the properties of the integrands of I, I_0, and I_1. ∎

A similar construction can be applied to ϕ to obtain $\phi_{\eta_0,\eta_1,\eta_2}$.

3.2. Derivation of the integral equation.

3.2.1. General notation. In this subsection we introduce general notation and operators which will be used in the construction, discretization, and solution of our boundary integral equations.

Given a point $\mathbf{x}_0 \in \partial\Omega$, let $\hat{\mathbf{n}}(\mathbf{x}_0)$ denote the outward pointing normal of $\partial\Omega$ at $\mathbf{x}_0$. Similarly, relative to that normal, let $\kappa_1(\mathbf{x}_0)$ and $\kappa_2(\mathbf{x}_0)$ denote the principal curvatures of $\partial\Omega$ at $\mathbf{x}_0$, the quantities $\mathcal{H}(\mathbf{x}_0)$, $\mathcal{Q}(\mathbf{x}_0)$ denote their sums and differences and let $\hat{\mathbf{t}}_1(\mathbf{x}_0)$, $\hat{\mathbf{t}}_2(\mathbf{x}_0)$ be the principal directions. For ease of exposition, when there is no risk of confusion we will frequently omit the subscripts. In the following, it will be convenient to work in the rotated and shifted coordinate frame $\mathbf{x} - \mathbf{x}_0 = u\,\hat{\mathbf{t}}_1(\mathbf{x}_0) + v\,\hat{\mathbf{t}}_2(\mathbf{x}_0) + q\,\hat{\mathbf{n}}(\mathbf{x}_0)$.

For $\eta_2 < \eta_1 < \eta_0 < 0$, we define the functions

$$\begin{aligned} Q^{\pm}_{\eta_0,\eta_1,\eta_2}(u,v,q;\mathbf{x}_0) = \frac{1}{2\pi|\mathbf{x}-\mathbf{x}_0|} &\mp \frac{\mathcal{H}(\mathbf{x}_0)}{4\pi} \phi_{\pm\eta_0,\pm\eta_1,\pm\eta_2}(u,v,\pm q) \\ &\pm \frac{\mathcal{Q}(\mathbf{x}_0)}{8\pi} \psi_{\pm\eta_0,\pm\eta_1,\pm\eta_2}(u,v,\pm q). \end{aligned}$$

For Q^+, the exterior function, η_0, η_1, and η_2 should be chosen so that $\mathbf{x}_0 + \eta_2 \hat{\mathbf{n}}(\mathbf{x}_0)$ is in the interior of Ω, preferably far away from the boundary. For Q^-, the interior function, they should be chosen so that $\mathbf{x}_0 - s\hat{\mathbf{n}}(\mathbf{x}_0) \in \Omega$ for $\eta_2 \le s \le 0$. We note that for many geometry/source configurations, these 'image points' can be omitted entirely for the interior problem.

Given a density $\sigma \in L^2(\partial\Omega)$, we define the standard single layer operator S (see [34] for example) by

$$S[\sigma](\mathbf{x}) = \int_{\partial\Omega} G_F(\mathbf{x}-\mathbf{x}')\,\sigma(\mathbf{x}')\,\mathrm{d}A(\mathbf{x}'), \qquad G_F(\mathbf{x}) = \frac{1}{4\pi|\mathbf{x}|}.$$

When thinking of it as a map from $L^2(\partial\Omega) \to L^2(\partial\Omega)$ we denote it by $\mathcal{S}$. It is well-known, see [34] for example, that for $\sigma \in L^2(\partial\Omega)$, the normal limit of the normal derivative of S exists, in an L^2 sense, and

$$\lim_{\epsilon\to 0} \hat{\mathbf{n}}(\mathbf{x}) \cdot \nabla S[\sigma](\mathbf{x} \pm \epsilon\,\hat{\mathbf{n}}(\mathbf{x})) = \mp\frac{1}{2}\sigma(\mathbf{x}) + \text{p.v.} \int_{\partial\Omega} \hat{\mathbf{n}}(\mathbf{x}) \cdot \nabla_{\mathbf{x}} G_F(\mathbf{x}-\mathbf{x}')\,\sigma(\mathbf{x}')\,\mathrm{d}A(\mathbf{x}').$$

The integral on the right-hand side is weakly-singular and so the principal value can be dropped. For $\sigma \in L^2(\partial\Omega)$ we let $\mathcal{S}' : L^2(\partial\Omega) \to L^2(\partial\Omega)$ denote the operator defined by

$$\mathcal{S}'[\sigma](\mathbf{x}) = \int_{\partial\Omega} \hat{\mathbf{n}}(\mathbf{x}) \cdot \nabla_{\mathbf{x}} G_F(\mathbf{x}-\mathbf{x}')\,\sigma(\mathbf{x}')\,\mathrm{d}A(\mathbf{x}').$$

3.2.2. The exterior problem. When solving the exterior problem we consider the ansatz

$$G^e(\mathbf{x};\mathbf{x}_0) = Q^+_{\eta_0,\eta_1,\eta_2}(\mathbf{x};\mathbf{x}_0) + S[\sigma_{\mathbf{x}_0}](\mathbf{x})$$

where $\sigma_{\mathbf{x}_0}$ is some yet to be determined density. Note that by construction G^e is harmonic in the exterior region $\mathbb{R}^3 \setminus \Omega$. Taking the normal limit of the normal derivative of G^e, and inserting it into our boundary condition, we obtain the integral equation

$$-\frac{1}{2}\sigma_{\mathbf{x}_0}(\mathbf{x}) + \mathcal{S}'[\sigma_{\mathbf{x}_0}](\mathbf{x}) = -\partial_n Q^+_{\eta_0,\eta_1,\eta_2}(\mathbf{x};\mathbf{x}_0). \tag{3.5}$$

Here, $\partial_n Q^+$ denotes the normal derivative of Q^+ on surface, i.e. excluding the delta function. Standard results give existence and uniqueness for (3.5), see [34] for example.

3.2.3. The interior problem. Turning to the interior problem, we use the ansatz

$$G^i(\mathbf{x};\mathbf{x}_0) = Q^-_{\eta_0,\eta_1,\eta_2}(\mathbf{x};\mathbf{x}_0) + S[\sigma_{\mathbf{x}_0}](\mathbf{x}) + \frac{u^2+v^2}{4|\Omega|} + \frac{\beta}{|\Omega|},$$

where again $\sigma_{\mathbf{x}_0}$ is some yet to be determined density and β is constant. The first term contributes the required delta function to $\partial_n G^i(\mathbf{x};\mathbf{x}_0)$ near $\mathbf{x} = \mathbf{x}_0$ and the third term enforces the constraint $\Delta G^i = 1/|\Omega|$ in Ω. If we again take the normal limit of the normal derivative of G^i, and insert it into our boundary condition, we obtain the integral equation

$$\frac{1}{2}\sigma_{\mathbf{x}_0}(\mathbf{x}) + \mathcal{S}'[\sigma_{\mathbf{x}_0}](\mathbf{x}) = -\partial_n Q^-_{\eta_0,\eta_1,\eta_2}(\mathbf{x};\mathbf{x}_0) - \frac{1}{|\Omega|}\partial_n p(\mathbf{x}), \tag{3.6}$$

with $p(\mathbf{x}) = (u^2+v^2)/4$. The operator on the left-hand side of the above equation has a one-dimensional nullspace. Indeed, it is easily shown [34] that for any $\mu \in L^2(\partial\Omega)$,

$$\int_{\partial\Omega} \mathcal{S}'[\mu](\mathbf{x})\,\mathrm{d}A(\mathbf{x}) = -\frac{1}{2}\int_{\partial\Omega}\sigma(\mathbf{x})\,\mathrm{d}A(\mathbf{x}),$$

i.e. constant functions are in the left nullspace. Consistency of the integral equation then requires

$$\int_{\partial\Omega}\left[\partial_n Q^-_{\eta_0,\eta_1,\eta_2}(\mathbf{x};\mathbf{x}_0) + \frac{1}{|\Omega|}\partial_n p(\mathbf{x})\right]\mathrm{d}A(\mathbf{x}) = 0,$$

which follows from Green's theorem. To remove the nullspace, we impose the additional condition that $\int_{\partial\Omega}\sigma_{\mathbf{x}_0}(\mathbf{x})\,\mathrm{d}A(\mathbf{x}) = 0$. We then arrive at the integral equation

$$\frac{1}{2}\sigma_{\mathbf{x}_0}(\mathbf{x}) + \mathcal{S}'[\sigma_{\mathbf{x}_0}](\mathbf{x}) + \frac{1}{|\Omega|}\int_{\partial\Omega}\sigma_{\mathbf{x}_0}(\mathbf{x}')\,\mathrm{d}A(\mathbf{x}') = -\partial_n Q^-_{\eta_0,\eta_1,\eta_2}(\mathbf{x};\mathbf{x}_0) - \frac{1}{|\Omega|}\partial_n p(\mathbf{x}). \tag{3.7}$$

To satisfy the volume integral constraint (1.2a) on G^i, we require that

$$\beta = -\int_\Omega\left[Q^-(\mathbf{x}) + S[\sigma_{\mathbf{x}_0}](\mathbf{x}) + \frac{u^2+v^2}{4|\Omega|}\right]\mathrm{d}V(\mathbf{x}).$$

To simplify the right-hand side, we note that $\Delta p = 1$, and by integrating by parts,

$$\begin{aligned}
\beta &= -\int_\Omega \underbrace{\Delta p}_{=1}\left[Q^-(\mathbf{x}) + S[\sigma_{\mathbf{x}_0}](\mathbf{x}) + \frac{u^2+v^2}{4|\Omega|}\right]\mathrm{d}V(\mathbf{x}) \\
&= -\int_{\partial\Omega}\partial_n p\left[Q^-(\mathbf{x}) + S[\sigma_{\mathbf{x}_0}](\mathbf{x}) + \frac{u^2+v^2}{4|\Omega|}\right]\mathrm{d}A(\mathbf{x}) \\
&\quad + \int_{\partial\Omega} p(\mathbf{x})\partial_n G(\mathbf{x};\mathbf{x}_0)\,\mathrm{d}A(\mathbf{x}) - \frac{1}{|\Omega|}\int_\Omega p(\mathbf{x})\,\mathrm{d}V(\mathbf{x}).
\end{aligned}$$

Using the fact that $\partial_n G^i(\mathbf{x};\mathbf{x}_0) = -\delta(\mathbf{x}-\mathbf{x}_0)$ we see that since $p(\mathbf{x}_0) = 0$, the second term on the right-hand side of the above equation vanishes. Additionally, $p(\mathbf{x}) = \nabla\cdot\frac{1}{12}(\hat{\mathbf{t}}_1(\mathbf{x}_0)u^3 + \hat{\mathbf{t}}_2(\mathbf{x}_0)v^3)$, so the last integral in the above expression can be computed via a boundary integral. Putting this all together, the condition for β may be written in the form

$$\beta = -\gamma - \int_{\partial\Omega}\sigma_{\mathbf{x}_0} S[\partial_n p](\mathbf{x})\,\mathrm{d}A(\mathbf{x}),$$

where we have applied Fubini's theorem to the integral and

$$\gamma = \int_{\partial\Omega}\left[\partial_n p\Big[Q^-(\mathbf{x};\mathbf{x}_0) + \frac{u^2+v^2}{4|\Omega|}\Big] + \frac{1}{|\Omega|}\hat{\mathbf{n}}(\mathbf{x})\cdot\frac{1}{12}\Big(\hat{\mathbf{t}}_1(\mathbf{x}_0)u^3 + \hat{\mathbf{t}}_2(\mathbf{x}_0)v^3\Big)\right]\mathrm{d}A(\mathbf{x}).$$

Note that despite the singularities in Q^-, the integrand vanishes at $\mathbf{x}_0$.

REMARK. *In [9], a slightly different formulation is given. In essence, in that paper the constant term β is determined at the same time as the density $\sigma_{\mathbf{x}_0}$. In this work we first compute $\sigma_{\mathbf{x}_0}$ and then obtain β afterwards in the postprocessing step.*

REMARK. *For off-surface sources, either exterior or interior, the singular part of the Neumann Green's function is simply the free-space Laplace Green's function, and the regular part has smooth normal derivatives on $\partial\Omega$. For the exterior problem, the regular part can be obtained by using the ansatz $G(\mathbf{x};\mathbf{x}_0) = G_F(\mathbf{x}-\mathbf{x}_0) + S[\sigma_{\mathbf{x}_0}](\mathbf{x})$ and solving (3.5) with a different right hand side (see [34] for more details). For the interior problem, we use the ansatz $G(\mathbf{x};\mathbf{x}_0) = G_F(\mathbf{x}-\mathbf{x}_0) + S[\sigma_{\mathbf{x}_0}](\mathbf{x}) + \frac{|\mathbf{x}|^2}{6|\Omega|} + \frac{\beta}{|\Omega|}$, solve (3.7) with the corresponding right hand side, and compute β as before (see [9] for more details).*

3.3. Discretization of the integral equations. In this paper we use a standard collocation method for the efficient discretization and solution of the integral equations (3.5) and (3.7), which are both of the general form

$$\sigma + K[\sigma] = f. \tag{3.8}$$

To make the presentation as self-contained as possible we briefly sketch the main idea of the approach. We refer the interested reader to [27] for more details and references, and to the software package *fmm3dbie* [2] which we have used in our numerical illustrations.

3.3.1. Discretization of the equations. In the following we let T_0 denote the standard right-triangle $T_0 = \{(x,y) \in \mathbb{R}^2_{>0} \,|\, x+y<1\}$ and assume that the boundary of Ω is specified via a union of smooth mutually-disjoint maps $\phi_j : T_0 \to \partial\Omega$, with $j = 1,\ldots,N_{\text{patches}}$. Let T_j denote the image of T_0 under ϕ_j.

The integral equation (3.8) can then be written as

$$\sigma(\mathbf{x}) + \sum_{j=1}^{N_{\text{patches}}} \int_{T_0} K(\mathbf{x},\phi_j(u,v))\,\sigma(\phi_j(u,v))\,|\,g_j(u,v)|\,\mathrm{d}A(u,v) = f(\mathbf{x}), \tag{3.9}$$

where g_j denotes the determinant of the metric tensor of the j^{th} patch which we assume to be boundedly invertible on the closure of T_0.

Next, we fix a basis $\tau_k : T_0 \to \mathbb{R}$, $k = 1,\ldots,N_{\text{basis}}$, and let $\{(u_k,v_k)\}_{k=1}^{N_{\text{basis}}} \subset T_0$ be an associated set of discretization nodes. Typically, we assume that the nodes are constructed so that the coefficients-to-values matrix $V_{k,\ell} := \{\tau_\ell(u_k,v_k)\}_{k,\ell=1}^{N_{\text{basis}}}$ is as well-conditioned as possible. We then relax (3.9), instead only requiring consistency at our discretization nodes,

$$\sigma_i(u_k,v_k) + \sum_{j=1}^{N_{\text{patches}}} \int_{T_0} K(\phi_i(u_k,v_k),\phi_j(u,v))\,\sigma_j(u,v)\,|g_j|\,\mathrm{d}A = f_i(u_k,v_k), \tag{3.10}$$

where $\sigma_i(u,v) = \sigma(\phi_i(u,v))$ and $f_i(u,v) = f(\phi_i(u,v))$. Assuming that σ_i is approximately in the span of the basis functions τ_k, then

$$\sigma_i(u,v) \approx \sum_{j=1}^{N_{\text{basis}}} \tau_j(u,v)(V^{-1})_{j,k}\sigma_i(u_k,v_k),$$

which we can insert into (3.10) to obtain

$$\sigma_{i,k} + \sum_{j=1}^{N_{\text{patches}}}\sum_{\ell=1}^{N_{\text{basis}}} K_{i,k,j,\ell}\sigma_{j,\ell} \approx f_{i,k}, \qquad i = 1,\ldots,N_{\text{patches}}; \quad k = 1,\ldots,N_{\text{basis}}, \tag{3.11}$$

with $\sigma_{i,k} = \sigma_i(u_k,v_k)$, $f_{i,k} = f_i(u_k,v_k)$ and

$$K_{i,k,j,\ell} = \sum_{m=1}^{N_{\text{basis}}} (V^{-1})_{m,\ell} \int_{T_0} K(\phi_i(u_k,v_k),\phi_j(u,v))\,\tau_m(u,v)\,|g_j|\,\mathrm{d}A. \tag{3.12}$$

In this paper, except for the patches touching $\mathbf{x}_0$, we choose the basis on T_0 to be Koornwinder polynomials of degree at most N_{order}, which give an orthonormal basis of the monomials $u^j v^k$, $j,k \geq 0$, $j+k \leq N_{\text{order}}$ on T_0 (we defer discussion of the near-$\mathbf{x}_0$ patches to Section 3.3.6). With this choice, $N_{\text{basis}} = (N_{\text{order}}+1)(N_{\text{order}}+2)/2$. For the corresponding discretization nodes, we use the N_{order} Vioreanu-Rokhlin (VR) nodes [52], which are chosen so as to give a well-conditioned V matrix. Associated with the VR nodes (u_j, v_j) is a set of quadrature weights $\{w_j\}_{j=1}^{N_{\text{basis}}}$ such that the quadrature rule with nodes (u_j, v_j) and weights w_j integrate all Koornwinder polynomials of degree at most N_{order} exactly.

3.3.2. Quadrature for weakly-singular integral operators. The remaining piece is the numerical calculation of the integrals $K_{i,k,j,\ell}$ in (3.12). Here we give a brief sketch of the approach taken in *fmm3dbie*, more details of which can be found in [27]. Broadly speaking, for a given *target* patch number i we split the *source* patches $j = 1, \ldots, N_{\text{patches}}$ into three sets: self ($i = j$), near patches ($i \neq j$ but the i^{th} patch is 'close' to the j^{th} patch), and far (patches which are neither self nor near). In our numerical experiments we use the default settings of *fmm3dbie* [2, 5, 53].

3.3.3. Far quadrature. When the source patch T_j is a sufficient distance from the target patch T_k, the kernel $K(\phi_i(u_k, v_k), \phi_j(u, v))$ is in $C^\infty(\overline{T_0})$, as is $\sqrt{|g_j|}$. For these integrals we use the *native quadrature rule*,

$$K_{i,k,j,\ell} \approx \sum_{n=1}^{N_{\text{basis}}} \sum_{m=1}^{N_{\text{basis}}} \left[K(\phi_i(u_k, v_k), \phi_j(u_m, v_m)) \tau_n(u_m, v_m) \left|\det g_j(u_m, v_m)\right| \, w_m\right] (V^{-1})_{n,\ell}, \tag{3.13a}$$

$$\approx \sum_{m=1}^{N_{\text{basis}}} \left[K(\phi_i(u_k, v_k), \phi_j(u_m, v_m)) \left|\det g_i(u_m^i, v_m^i)\right| \, w_m\right], \tag{3.13b}$$

where we have used the definition of V in going from the first line to the second.

Remark. *In practice the above integrals are frequently computed using oversampling: integrals are computing using a Vioreanu-Rokhlin quadrature rule that is higher order than the order of the polynomial expansions. In most settings, it is infeasible to assume that one has an analytic description of the surface available at the time when matrix entries are being computed. We describe how to address this in the next section.*

3.3.4. Near quadrature. For source patches T_j lying close to the target patch T_i, the kernel K will be nearly-singular, and so its coefficients when expressed in the Koornwinder polynomial basis will decay extremely slowly, if at all. In this case, the native quadrature rule, or the oversampling procedure alluded to in Remark 3, will not be accurate enough without an impractical number of nodes. Instead, we use adaptive integration, subdividing the patch T_j into smaller patches recursively until the error is within a prescribed tolerance. In practice, when splitting patches one rarely has access to an analytic description of the surface to query. Instead, the maps ϕ_j are approximated by maps $\hat{\phi}_j$ given by Koornwinder polynomial expansions. In particular, we represent our surface $\partial\Omega$ by storing the values of ϕ_j, $\partial_u \phi_j$, $\partial_v \phi_j$, and other surface properties (normals, shape operators, etc.) at Vioreanu-Rokhlin nodes (u_k, v_k) for each patch. If, when the surface is being constructed, the derivatives of the maps ϕ_j are not given analytically, then approximations are computed via numerical differentiation. With these approximate maps $\hat{\phi}_j$, we can interpolate relevant geometric quantities to any point in T_0. We refer the interested reader to [27] for a more thorough discussion of this procedure and its attendant considerations.

3.3.5. Self quadrature. For the self quadrature, when the source patch and the target patch are the same, once again the singularities of K preclude using the native quadrature rule, though adaptive integration, as for the near quadrature, can still be used. In practice, since many levels of refinement are required for adaptive integration on self patches, this can become prohibitively slow. Instead, a standard approach is to use *generalized Gaussian quadratures* [5], which uses preconstructed tables of specially constructed quadrature rules which are designed to integrate functions with singularities like those found in our kernels. We refer the reader to [5, 27] for a detailed description of these quadratures and their use.

3.3.6. Singularities in the right-hand sides. For smooth domains and smooth right-hand sides, the above discretization and quadrature procedure yields high-order convergence, and can be easily coupled to standard fast algorithms such as the fast multipole method (FMM) [28] and fast direct solvers [40, 29].

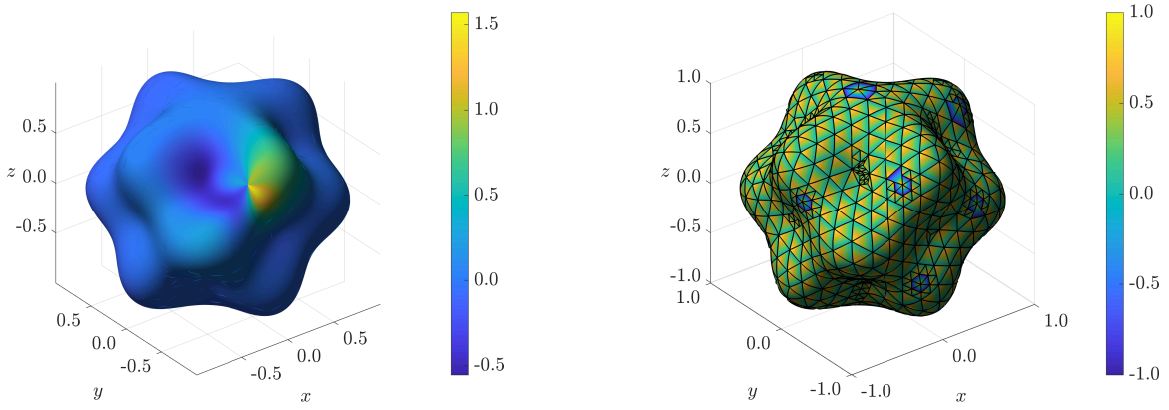

(a) Right hand side of (3.6): $-\partial_n Q^-(\mathbf{x};\mathbf{x}_0) - \frac{1}{|\Omega|}\partial_n p(\mathbf{x})$.

(b) Second coordinate $v \in (0,1)$ or $t \in (-1,1)$ on each patch.

Fig. 3.1: Example right hand side and discretization for a sphere with a radius that has been perturbed by a spherical harmonic, $0.3 \cdot \Re Y_6^4$. Left: An example right hand side for (3.6), which has a singularity at the source $\mathbf{x}_0 = (-0.2910, -0.8131, 0.5674) \in \partial\Omega$. Right: The orientation of our mesh elements. In this discretization, we have introduced a few collections of Duffy patches, so that the same quadratures can be used to compute $G(\mathbf{x};\mathbf{x}_0)$ for multiple $\mathbf{x}_0$.

When sources are present on the boundary, however, the right-hand side contains $\partial_n Q^{\pm}_{\eta_0,\eta_1,\eta_2}$ which is not smooth in the vicinity of $\mathbf{x}_0$ (see Fig. 3.1(a)). More specifically, it is easily seen that the right-hand side is smooth (except for a removable singularity) on any smooth curve passing through the source $\mathbf{x}_0$. The limiting behavior as $\mathbf{x} \to \mathbf{x}_0$, however, depends on the direction of approach. To see this, we note that the images at $\mathbf{x}_0 + \eta_j \hat{\mathbf{n}}(\mathbf{x}_0)$ for $j = 0, 1, 2$ contribute a smooth term to $\partial_n Q^{\pm}_{\eta_0,\eta_1,\eta_2}$. The remaining piece can be expressed as a ratio of smooth functions of μ and ν, whose limiting behavior is given by the right hand side of (2.13b) as $\mathbf{x} \to \mathbf{x}_0$.

This singularity presents two difficulties. Firstly, neither the density nor the right-hand side are well-represented in a piecewise polynomial basis, leading to slow convergence. Secondly, the formula for $\partial_n Q^{\pm}$ involves cancellations between singular terms which, if computed naively, give rise to catastrophic cancellations. Here we summarize our approach for overcoming these issues.

The first step is to ensure that the source $\mathbf{x}_0$ coincides exactly with a vertex of the triangulation of $\{T_i\}$. This can be easily done with standard meshing tools such as Gmsh [22] or distmesh [44]. Let $\mathcal{I}$ be the set of indices i for which the corresponding triangle T_i in the mesh has a vertex at $\mathbf{x}_0$. For convenience, we assume that these patches are oriented so that $\phi_i(0,1) = \mathbf{x}_0$ for $i \in \mathcal{I}$. For each θ, $\boldsymbol{r}_\theta(r) := \phi_i(r\cos\theta, 1 - r\sin\theta)$ is a curve passing through $\mathbf{x}_0$ that smoothly depends on θ. The above discussion then implies that $\partial_n Q^{\pm}_{\eta_0,\eta_1,\eta_2}(\phi_i(r\cos\theta, 1 - r\sin\theta))$ will be a smooth function of r and θ for each $i \in \mathcal{I}$. As mentioned above, the polar singularity prevents $\partial_n Q^{\pm}_{\eta_0,\eta_1,\eta_2} \circ \phi_i$ from being well represented by the basis of Koornwinder polynomials. Instead, we introduce the Duffy transform [20]

$$\psi(s,t) = \left(\frac{s+1}{2}\frac{1-t}{2},\ \frac{t+1}{2}\right),$$

which is a bijection from the square $(-1,1)^2$ into T_0. This parameterization is chosen so that the lines of constant s are mapped to different straight lines passing through the point $(0,1)$. Thus

$$\partial_n Q^{\pm}_{\eta_0,\eta_1,\eta_2} \circ \phi_i \circ \psi(s,t),$$

will be a smooth function of $(s,t) \in (-1,1)^2$. It can therefore be well represented in the basis $\tilde{\tau}_{k,k'}(s,t) := P_k(s)P_{k'}(t)$ with $k, k' = 1, \ldots, N_{\text{order}} + 1$ of tensor product Gauss-Legendre polynomials. With this in mind,

on the square $(-1,1)^2$ we choose our discretization points to be tensor products of Gauss-Legendre nodes: $\{(s_k, s_{k'})\}_{k,k'=1}^{N_{\text{order}}+1}$. An example of the patch orientation is shown in Fig. 3.1(b). With this choice of basis function and discretization nodes, the discretization and quadrature scheme summarized in Sections 3.3.1-3.3.5 can be extended *mutatis mutandis* to accommodate these modified patches, though we choose the order of these 'Duffy' patches to be four higher than the order of triangular patches. Extensive numerical evidence suggests that the density σ is also well-resolved on the Duffy patches.

The addition of Duffy patches enables high-order convergence, even near the source, and so eliminates the need for excessive refinement of the patches near the source. This, in turn, reduces the effect of catastrophic cancellations, since quadrature nodes on the larger Duffy patches the right-hand side are typically farther from the source than nodes would be if many levels of refinement were used. Still, for high accuracy and robustness, care is required when evaluating $\partial_n Q^{\pm}_{\eta_0,\eta_1,\eta_2}$ at nodes close to $\mathbf{x}_0$, as the expression contains a difference of singular terms. Specifically, it can be expressed as a sum of bounded terms plus a term of the form

$$\frac{\hat{\mathbf{n}}(\mathbf{x})\cdot(\mathbf{x}-\mathbf{x}_0)}{2\pi|\mathbf{x}-\mathbf{x}_0|^3} - \frac{\kappa_1+\kappa_2}{8\pi}\frac{1}{|\mathbf{x}-\mathbf{x}_0|} - \frac{\kappa_1-\kappa_2}{8\pi}\frac{p_1^2-p_2^2}{|\mathbf{x}-\mathbf{x}_0|^3} = \frac{\hat{\mathbf{n}}(\mathbf{x})\cdot(\mathbf{x}-\mathbf{x}_0) - \frac{1}{2}\kappa_1 p_1^2 - \frac{1}{2}\kappa_2 p_2^2 + O(|\mathbf{x}-\mathbf{x}_0|^4)}{2\pi|\mathbf{x}-\mathbf{x}_0|^3}.$$

While the $O(|\mathbf{x}-\mathbf{x}_0|^4)$ term in the numerator can be easily evaluated without catastrophic cancellations, the cancellation of the first three terms in the numerator is fairly delicate. Let

$$F(s,t) = \hat{\mathbf{n}}(s,t)\cdot(\mathbf{x}(s,t)-\mathbf{x}_0) - \frac{1}{2}\kappa_1 p_1(s,t)^2 - \frac{1}{2}\kappa_2 p_2(s,t)^2.$$

To stably evaluate F, we note that that $F(s,1) = \partial_t F(s,1) = \partial_t^2 F(s,1) = 0$ [30], and hence

$$F(s,t) = -\int_t^1 \frac{1}{2}(t-t')^2 \partial_t^3 F(s,t')\,\mathrm{d}t'. \tag{3.14}$$

This formula explicitly uses the fact that $F = O(|\mathbf{x}-\mathbf{x}_0|^3)$ and does not involve cancellations, and so gives a stable way for computing the most singular part of $\partial_n Q^{\pm}_{\eta_0,\eta_1,\eta_2}$. We discretize the integral in (3.14) using a 16th order Gauss-Legendre rule. In order to evaluate the integrand, we use the parameterization or implicit function defining our surface to compute $\partial_t^3 F$ at the nodes $(s_k, s_{k'})$. We then interpolate it to the required positions. For surfaces, where the required derivatives are not known we instead approximate $\partial_t^3 F$ by differentiating the tensor product Legendre interpolant of F on the patch. While the accuracy of these numerically computed derivatives is limited, this approach still avoids the catastrophic cancellation inherent in F and enables a sufficiently accurate evaluation of $\partial_n Q^{\pm}_{\eta_0,\eta_1,\eta_2}$.

3.4. Derivatives with respect to source location. In many applications the computation of the Neumann Green's function, and its regular part, appear in an objective function in which the location of the source appears as a parameter to be optimized over. If gradients with respect to source locations are computed using finite difference, catastrophic cancellation can lead to loss of accuracy. Instead, one can obtain these derivatives directly from the integral equation. For sources which are off-surface (either in the interior or exterior), the right hand side f in the integral equation (3.8) is smooth, and can be differentiated in $\mathbf{x}_0$. The integral equation can then be discretized and solved 'as-is' with this modified right-hand side in order to compute the derivative of the solution with respect to $\mathbf{x}_0$.

For on-surface sources, differentiating $Q^{\pm}$ with respect to $\mathbf{x}_0$ leads to a more singular right-hand side. In principle this can be handled by changing the basis used to represent the density in the vicinity of the source. Computing the right-hand side would still require care to avoid catastrophic cancellations in the evaluation of the more singular data. An alternative approach is to use reciprocity. In particular, if $\mathbf{x}, \mathbf{x}_0 \in \partial\Omega$, $\mathbf{x} \neq \mathbf{x}_0$, Green's identities give

$$G(\mathbf{x};\mathbf{x}_0) = G(\mathbf{x}_0;\mathbf{x}).$$

Hence, $\nabla_{\mathbf{x}_0} G(\mathbf{x};\mathbf{x}_0) = \nabla_{\mathbf{x}_0} G(\mathbf{x}_0;\mathbf{x})$. Derivatives with respect to the target do not change the right-hand side or the solution of (3.8), and appear only in the post-processing to evaluate the field.

4. Results. In this section we demonstrate our method on a variety of examples and benchmark against several scenarios where closed form or highly accurate solutions of (1.1) and (1.2) are available.

4.1. Sphere. For the unit sphere, closed form solutions for both the interior and exterior Green's functions are available.
Interior bulk: For $\mathbf{x} \in \Omega$, $\mathbf{x}' = \mathbf{x}/|\mathbf{x}|^2$ and $\mathbf{x}_0 \in \Omega$, we have that (see [14, Appendix A])

$$G^i(\mathbf{x};\mathbf{x}_0) = \frac{1}{4\pi|\mathbf{x}-\mathbf{x}_0|} + R^i(\mathbf{x};\mathbf{x}_0), \tag{4.1a}$$

$$R^i(\mathbf{x};\mathbf{x}_0) = \frac{1}{4\pi|\mathbf{x}||\mathbf{x}'-\mathbf{x}_0|} + \frac{1}{4\pi}\log\left[\frac{2}{1-\mathbf{x}\cdot\mathbf{x}_0+|\mathbf{x}||\mathbf{x}'-\mathbf{x}_0|}\right] + \frac{1}{8\pi}\left(|\mathbf{x}|^2+|\mathbf{x}_0|^2\right) - \frac{7}{10\pi}. \tag{4.1b}$$

Interior surface: For $\mathbf{x}_0 \in \partial\Omega$ and $\mathbf{x} \in \Omega$, we have that [15, Lemma 2.1]

$$G^i(\mathbf{x};\mathbf{x}_0) = \frac{1}{2\pi|\mathbf{x}-\mathbf{x}_0|} + \frac{1}{4\pi}\log\left(\frac{2}{1-\mathbf{x}\cdot\mathbf{x}_0+|\mathbf{x}-\mathbf{x}_0|}\right) + \frac{1}{8\pi}\left(|\mathbf{x}|^2+1\right) - \frac{7}{10\pi}. \tag{4.2a}$$

In the limit as $\mathbf{x} \to \mathbf{x}_0$, the regular part can be identified to be

$$R^i(\mathbf{x}_0;\mathbf{x}_0) = \frac{1}{4\pi}\log 2 - \frac{9}{20\pi}. \tag{4.2b}$$

Exterior surface: For $\mathbf{x}_0 \in \partial\Omega$ and $\mathbf{x} \in \mathbb{R}^3 \setminus \Omega$, we have that (cf. [42])

$$G^e(\mathbf{x};\mathbf{x}_0) = \frac{1}{2\pi|\mathbf{x}-\mathbf{x}_0|} - \frac{1}{4\pi}\log\left(\frac{1-\mathbf{x}\cdot\mathbf{x}_0+|\mathbf{x}-\mathbf{x}_0|}{|\mathbf{x}|-\mathbf{x}\cdot\mathbf{x}_0}\right). \tag{4.3a}$$

In the limit as $\mathbf{x} \to \mathbf{x}_0$, we identify from (4.3a) that the exterior regular part is

$$R^e(\mathbf{x}_0;\mathbf{x}_0) = -\frac{1}{4\pi}\log 2. \tag{4.3b}$$

In Fig. 4.1 we display relative errors between these known exact solutions and our numerical method. In Fig. 4.1(a) we plot the interior solution $R^i(\mathbf{x};\mathbf{x}_0)$ for $\mathbf{x}_0 = (-\frac{1}{4}, \frac{1}{3}, -\frac{1}{5})$ where $\mathbf{x}$ are points lying on a plane through the origin. The relative error is approximately 10^{-12}. In Fig. 4.1(b), we plot the relative errors in the approximation of $R^i(\mathbf{x}_0;\mathbf{x}_0)$ and $R^e(\mathbf{x}_0;\mathbf{x}_0)$, given by (4.2b) and (4.3b) respectively, along an arc of points $\mathbf{x}_0 = (\sqrt{1-\eta_0^2}, 0, \eta_0)$ for $\eta_0 \in [-1, 1]$. The numerical method provides an approximation of these values to a relative error of around 10^{-9}.

4.2. A family of axi-symmetric solutions for the exterior Green's function. In this section, we construct a family of domains and solutions for the exterior Green's function (1.1) and compare with our numerical method. Our strategy will be to first specify a harmonic function $G^e(\mathbf{x};\mathbf{x}_0)$ with the correct singularity structure at the source and then determine a domain Ω that satisfies the Neumann boundary condition (1.1a). Throughout the construction, the surface source is located at $\mathbf{x}_0 = (0, 0, 1) \in \partial\Omega$ which will generate an axi-symmetric solution.

We will work in axi-symmetric spherical coordinates (d, θ) centered at the origin for which

$$d = \sqrt{r^2+z^2}\ , \qquad \theta = \tan^{-1}\left[\frac{r}{z}\right]\ , \tag{4.4}$$

where $r = \sqrt{x^2+y^2}$ is the distance to the polar axis. We define an orthonormal basis in the (r, z) plane,

$$\hat{\mathbf{d}} = (\sin\theta, \cos\theta)\ , \qquad \hat{\boldsymbol{\theta}} = (\cos\theta, -\sin\theta)\ ,$$

corresponding to radial and polar vectors and note that $\frac{\partial\hat{\mathbf{d}}}{\partial\theta} = \hat{\boldsymbol{\theta}}$. We also define cylindrical coordinates (r, η) centered at the source $\mathbf{x}_0 = (0, 0, 1)$ for convenience,

$$r = \sqrt{x^2+y^2} = d\sin\theta\ , \quad \eta = z-1\ ,$$

for which the distance to the source is given by

$$\rho = \sqrt{r^2+(z-1)^2} = \sqrt{d^2-2d\cos\theta+1}\ .$$

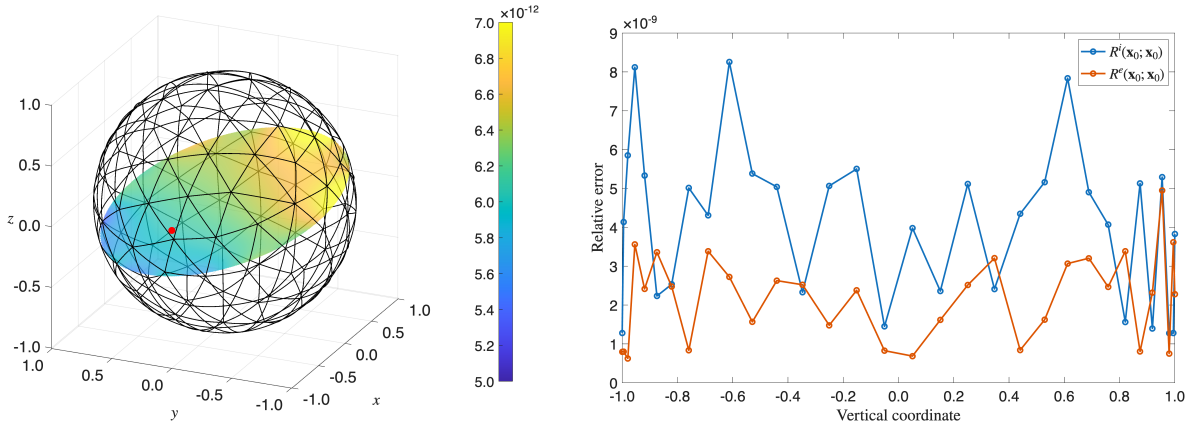

(a) $R^i(\mathbf{x};\mathbf{x}_0)$ for $\mathbf{x}_0 \in \Omega$.

(b) Relative errors in $R^e(\mathbf{x}_0;\mathbf{x}_0)$ and $R^i(\mathbf{x}_0;\mathbf{x}_0)$ for $\mathbf{x}_0 \in \partial\Omega$.

Fig. 4.1: Error in numerical approximation in the sphere case. Left: Relative error in calculation of $R^i(\mathbf{x};\mathbf{x}_0)$ for $\mathbf{x}_0 \in \Omega$ (red dot) and evaluated at points $\mathbf{x}$ on an interior plane through the origin. The relative error is around 5×10^{-12}. Right: Relative errors for numerical evaluation of $R^e(\mathbf{x}_0;\mathbf{x}_0) = -\frac{1}{4\pi}\log 2$ and $R^i(\mathbf{x}_0;\mathbf{x}_0) = \frac{1}{4\pi}\log 2 - \frac{9}{20\pi}$ for points $\mathbf{x}_0 = (\sqrt{1-\eta_0^2}, 0, \eta_0)$ and $\eta_0 = [-1, 1]$. The agreement is around 10^{-9}.

Motivated by the exact solution for the sphere case in section 4.1, we propose axi-symmetric solutions for $G^e(\mathbf{x};\mathbf{x}_0)$ and seek to find the domain

$$\Omega = \{\mathbf{x} \mid d \le P(\theta) \quad \text{for} \quad 0 \le \theta \le \pi\},$$

where $P(\theta)$ is to be determined. The conditions

$$P(0) = 1, \qquad P'(0) = P'(\pi) = 0,$$

place the source at the north pole of the surface and preclude a cusp at the north or south pole. The (un-normalized) tangent vector $\mathbf{t}(P)$ and normal vector $\mathbf{n}(P)$ to this curve are

$$\mathbf{t}(P) = P'(\theta)\hat{\mathbf{d}} + P(\theta)\hat{\boldsymbol{\theta}}, \qquad \mathbf{n}(P) = P(\theta)\hat{\mathbf{d}} - P'(\theta)\hat{\boldsymbol{\theta}}\ .$$

For a known Green's function $G^e(d,\theta)$, the boundary condition $\partial_n G^e = 0$ then becomes

$$\partial_n G^e = \left(G^e_d\,\hat{\mathbf{d}} + \frac{1}{d}G^e_\theta\,\hat{\boldsymbol{\theta}}\right)\cdot\left(P(\theta)\,\hat{\mathbf{d}} - P'(\theta)\,\hat{\boldsymbol{\theta}}\right) = 0, \qquad 0 \le \theta \le \pi. \tag{4.5}$$

If $G^e(d,\theta)$ is known, then (4.5) yields the following ODE for $P(\theta)$,

$$P'(\theta) = P^2\frac{G^e_d(P,\theta)}{G^e_\theta(P,\theta)}\ . \tag{4.6}$$

At the source, the surface has a local parameterization $\eta = \frac{\mathcal{H}}{2}r^2 + \mathcal{O}(r^4)$, for a smooth boundary with the prescribed mean curvature. As $\eta = z - 1 = P(\theta)\cos\theta - 1$ and $r = P(\theta)\sin\theta$, substituting and expanding yields

$$P(\theta) \sim 1 + \frac{1+\mathcal{H}}{2}\theta^2 + \mathcal{O}(\theta^4), \tag{4.7}$$

At the south pole ($\theta = \pi$) we want the surface to be smooth which implies $\lim_{\theta\to\pi} P'(\theta) = 0$. Moreover, the smoothness and axi-symmetry of the Green's function implies $\partial_\theta G^e(P,\pi) = 0$. From (4.6) we deduce that

$$\partial_d G^e(P,\pi) = 0\ ,$$

In practice, we find some d_* such that $\partial_d G(d_*,\pi) = 0$ which determines the location of the south pole and then enforce

$$\lim_{\theta\uparrow\pi} P(\theta) = d_*.$$

4.2.1. The proposed Green's function. Motivated by the spherical solution, we look for a surface with a specified G^e of the form

$$G^e(\mathbf{x};\mathbf{x}_0) = G^+(d,\theta) = \frac{1}{2\pi\rho} - \frac{\mathcal{H}}{4\pi}\log[\rho+\eta] - \frac{1}{4\pi d}[1+\mathcal{H}] + \frac{\mathcal{H}}{4\pi}\log[d+z]\ , \tag{4.8}$$

However, this form is singular on the polar axis for $z \le 1$ where $\rho + \eta = 0$. By noticing that $r^2 = \rho^2 - \eta^2 = d^2 - z^2$, one can see that

$$\frac{\rho-\eta}{d-z} = \frac{d+z}{\rho+\eta},$$

which allows us to derive an alternative form of $G^e(\mathbf{x};\mathbf{x}_0)$

$$G^e(\mathbf{x};\mathbf{x}_0) = G^-(d,\theta) = \frac{1}{2\pi\rho} + \frac{\mathcal{H}}{4\pi}\log[\rho-\eta] - \frac{1}{4\pi d}[1+\mathcal{H}] - \frac{\mathcal{H}}{4\pi}\log[d-z]\ , \tag{4.9}$$

which is valid everywhere except on the polar axis for $z \ge 0$. Patching these two solutions together yields

$$G^e(\mathbf{x};\mathbf{x}_0) = \begin{cases} G^+(d,\theta), & 0 \le \theta < \pi/2; \\ G^-(d,\theta), & \pi/2 \le \theta \le \pi. \end{cases} \tag{4.10}$$

which is C^∞ everywhere except for along the polar axis (where $r = 0$) when $0 \le z \le 1$. Along this line segment there is a singularity in the log terms and there is a source/sink at each endpoint of the line segment. These singularities are in the interior of Ω except for the expected singularity at $\mathbf{x} = \mathbf{x}_0$. Due to axisymmetry, we can write

$$z = d\cos\theta\ , \qquad \eta = d\cos\theta - 1\ , \qquad \rho = \sqrt{d^2 - 2d\cos\theta + 1}\ .$$

In the far-field

$$G^e(\mathbf{x};\mathbf{x}_0) \sim \frac{1}{4\pi d} + \frac{4+\mathcal{H}}{8\pi}\frac{\cos\theta}{d^2} + \mathcal{O}(1/d^3)\ ,$$

as $d \to \infty$ satisfying the far-field condition (1.1b). At the source $d = z = 1$,

$$G^e(\mathbf{x};\mathbf{x}_0) = \frac{1}{2\pi\rho} - \frac{\mathcal{H}}{4\pi}\log[\rho+\eta] - \frac{1}{4\pi}[1+\mathcal{H}] + \frac{\mathcal{H}}{4\pi}\log 2 + \mathcal{O}(\rho)\ .$$

which allows one to identify the regular part of the Green's function. We identify that the first two terms are the singular portion at the source,

$$G^e_{\text{sing}}(\mathbf{x};\mathbf{x}_0) = \frac{1}{2\pi\rho} - \frac{\mathcal{H}}{4\pi}\log[\rho+\eta],$$

and define $G^e(\mathbf{x};\mathbf{x}_0) \equiv G^e_{\text{sing}}(\mathbf{x};\mathbf{x}_0) + R^e(\mathbf{x};\mathbf{x}_0)$, then the last two terms yield the regular part,

$$R^e(\mathbf{x}_0;\mathbf{x}_0) = -\frac{1}{4\pi}[1+\mathcal{H}] + \frac{\mathcal{H}}{4\pi}\log 2\ . \tag{4.11}$$

On the positive polar axis $G^e(d,0) = G_+(d,0)$ is singular for $0 \le d \le 1$. For $d > 1$

$$G^e(d,0) = G_+(d,0) = -\frac{\mathcal{H}}{4\pi}\left[\log(1-1/d) + \frac{1}{d}\right] + \frac{d+1}{4\pi d(d-1)}, \qquad d > 1,$$

and as $d \downarrow 1$,

$$G^e_d(d,0) \sim -\frac{1}{2\pi}(d-1)^{-2}\ .$$

which is negative for all $\mathcal{H}$. At $\theta = \pi$,

$$G^e(d,\pi) = G_-(d,\pi) = \frac{\mathcal{H}}{4\pi}\left[\log(1+1/d) - \frac{1}{d}\right] + \frac{d-1}{4\pi d(d+1)}, \qquad d \ge 0,$$

and

$$G^e_d(d,\pi) = \frac{(\mathcal{H}+1)+(\mathcal{H}+2)d-d^2}{4\pi d^2(d+1)}.$$

The south pole of $\partial\Omega$ must be at a value d_* where the normal derivative vanishes, that is where $G^e_d(d_*,\pi)=0$. This yields

$$d_* = \frac{(\mathcal{H}+2) \pm \sqrt{\mathcal{H}^2+8\mathcal{H}+8}}{2}\ , \tag{4.12}$$

which has two real roots for $\mathcal{H} > \mathcal{H}_* \equiv -4+2\sqrt{2} \approx -1.17157$, a double root at this value and no solutions of smaller values of $\mathcal{H}$.

4.2.2. An implicit solution for the bounding domain. In this section we will use the fact that $G^e(d,\theta)$ is harmonic to derive an exact implicit solution of the ODE system (4.6) for $P(\theta)$. First note that for a harmonic function $\Delta G^e = 0$ (except for $0 \le d \le 1$ on the north polar axis) that

$$\Delta G^e \equiv \frac{1}{d^2}\frac{\partial}{\partial d}\Big(d^2\frac{\partial}{\partial d}G^e\Big) + \frac{1}{d^2\sin\theta}\frac{\partial}{\partial\theta}\Big(\sin\theta\frac{\partial}{\partial\theta}\,G^e\Big) = 0.$$

This can be rewritten as

$$\frac{\partial}{\partial d}\Big(d^2\sin\theta\,\frac{\partial}{\partial d}G^e\Big) + \frac{\partial}{\partial\theta}\Big(\sin\theta\,\frac{\partial}{\partial\theta}G^e\Big) = 0\ .$$

Now, rewriting the equation (4.6) for $P(\theta)$, we have that

$$\sin\theta\,\frac{\partial}{\partial\theta}G^e(P,\theta)\,\mathrm{d}P - P^2\sin\theta\,\frac{\partial}{\partial d}G^e(P,\theta)\,\mathrm{d}\theta = 0.$$

The differential equation $M(P,\theta)\,\mathrm{d}P + N(P,\theta)\,\mathrm{d}\theta = 0$ is exact if $M_\theta = N_P$ which is exactly the condition derived above. Integrating the equation yields the implicit solution

$$\frac{\mathcal{H}}{4\pi}\rho + \frac{1-P\cos\theta}{2\pi\rho} - \mathcal{H}\frac{P}{4\pi} + (1+\mathcal{H})\frac{\cos\theta}{4\pi} = C.$$

where

$$\rho = \sqrt{P^2-2P\cos\theta+1} = \sqrt{(1-P\cos\theta)^2+(P\sin\theta)^2},$$

is the distance to the source at the north pole. If we approach the north pole (that is we let $\rho\to 0$) with a behavior prescribed by (4.7) (that is $P \sim \frac{1+\mathcal{H}}{2}\theta^2$ as θ decreases to zero) we find that $C = \frac{1}{4\pi}$. The implicit definition of the surface can now be written as

$$F(P,\theta) = \mathcal{H}\rho + 2\frac{1-P\cos\theta}{\rho} - \mathcal{H}P + (1+\mathcal{H})\cos\theta - 1 = 0\ . \tag{4.13}$$

To find the south pole, expand $F(d_*,\pi-\varepsilon)=0$ as $\varepsilon\to 0$,

$$F(d_*,\pi-\varepsilon) \sim \frac{(\mathcal{H}+1)+(\mathcal{H}+2)d_*-d_*^2}{2(d_*+1)}\varepsilon^2 + \mathcal{O}(\varepsilon^4)\ .$$

This yields the same condition on d_* stated in (4.12).

We now summarize our process for generating a solution $G^e(\mathbf{x};\mathbf{x}_0)$ for $\mathbf{x}_0=(0,0,1)$ of (1.1). First we select a mean curvature $\mathcal{H} > \mathcal{H}_* \equiv -4+2\sqrt{2}$ and calculate the value d_* from (4.12). The exact Green's function $G^e(\mathbf{x};\mathbf{x}_0)$ is given by (4.10) and its regular part $R^e(\mathbf{x}_0;\mathbf{x}_0)$ by (4.11). For each $\theta\in[0,\pi]$, we solve the implicit equation $F(P,\theta)=0$ given in (4.13) for $P(\theta)$. The surface is then reconstructed from (4.4) for $d = P(\theta)$.

In Fig. 4.2 we demonstrate our process by constructing domains for a range of $\mathcal{H}$ values. The solution of the implicit equation (4.13) is shown in Fig. 4.2(b) which describes a family of "tear-drop" shaped domains. For each case, we use the constructed domain in our boundary integral method and evaluate the regular part $R^e(\mathbf{x}_0;\mathbf{x}_0)$. In Fig. 4.2(a) we show the constructed domain and a favorable comparison with the known value (4.11).

We remark that the choice of source placement $\mathbf{x}_0=(0,0,1)$ renders the solution axi-symmetric and hence $\mathcal{Q}(\mathbf{x}_0)=0$. Therefore the weaker singularity is not present in this example. This method can potentially be expanded to generate a larger class of domains by constructing more complex Green's functions from additional point sources. Despite some effort, we were not able to expand this methodology to generate domains without an axi-symmetric profile.

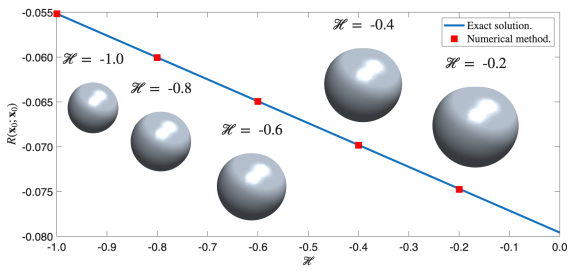

(a) The constructed domains and $R^e(\mathbf{x}_0;\mathbf{x}_0)$.

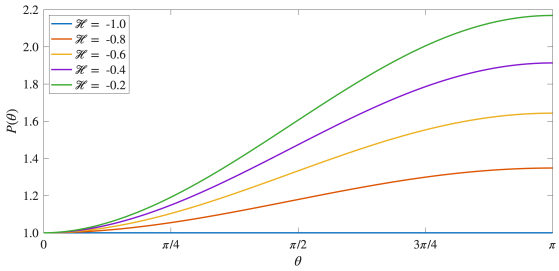

(b) The function $P(\theta)$.

Fig. 4.2: Comparison of the constructed solutions with the numerical method. For values $\mathcal{H} \in \{-1.0, -0.8, -0.6, -0.4, -0.2\}$ we construct the domain $P(\theta)$ from numerical solution of (4.6). The exact regular part $R^e(\mathbf{x}_0;\mathbf{x}_0)$ from (4.11) agrees closely with our numerical method (red squares).

4.3. Series solution in prolate spheroid harmonics. In this section, we develop a solution to the exterior surface Green's function (1.1) for the prolate spherical geometry defined by

$$\partial\Omega = \left\{ (x,y,z) \in \mathbb{R}^3 \;\middle|\; \frac{x^2+y^2}{a^2} + \frac{z^2}{b^2} = 1 \right\}, \tag{4.14}$$

where $b > a > 0$. The solution of (1.1) is separable in the prolate spheroid coordinate system

$$x = f\sqrt{(\xi^2-1)(1-\eta^2)}\cos\phi, \qquad y = f\sqrt{(\xi^2-1)(1-\eta^2)}\sin\phi, \qquad z = f\,\xi\,\eta, \tag{4.15}$$

where $f = \sqrt{b^2-a^2}$ is half the interfocal distance. Here $\xi \in [1,\infty)$ is the radial variable, $\eta \in [-1,1]$ is the elevation coordinate and $\phi \in [0,2\pi)$ is the azimuthal variable. The surface of the prolate spheroid is defined by the surface $\xi_0 = b/f$ and $\xi = 1$ is the line connecting the foci. The task is to solve for the Green's function and then peel off the triple singularity structure (1.5) to identify the regular part $R^e(\mathbf{x}_0;\mathbf{x}_0)$. We begin by recalling that the harmonic functions in prolate coordinates are

$$\{Q_n^m(\xi), P_n^m(\xi)\} \times \{P_n^m(\eta)\cos m\phi, P_n^m(\eta)\sin m\phi\},$$

for $n = 0, 1, \ldots$ and $m = 0, 1, \ldots, n$. Here P_n^m and Q_n^m are the associated Legendre functions of the first and second kind respectively [55, 54]. The functions $P_n^m(\xi)$ are unbounded as $\xi \to \infty$ while $Q_n^m(\xi)$ are bounded as $\xi \to \infty$. When restricted to $\xi = \xi_0$, the surface prolate spherical harmonics are the functions

$$C_n^m(\eta,\phi) = P_n^m(\eta)\cos m\phi, \qquad S_n^m(\eta,\phi) = P_n^m(\eta)\sin m\phi.$$

To establish the orthogonality structure, we introduce the weighted surface inner product

$$\langle u, v\rangle_w = \int_{\partial\Omega} u(\eta,\phi)v(\eta,\phi)\,w\,\mathrm{d}A, \qquad w = \frac{1}{f^2\sqrt{(\xi^2-\eta^2)(\xi^2-1)}},$$

for $\mathrm{d}A = w^{-1}\mathrm{d}\eta\,\mathrm{d}\phi$. The orthogonality relationships for the surface prolate harmonics are

$$\left\langle S_n^m, S_N^M \right\rangle_w = \gamma_{m,n}\delta_{n,N}\delta_{m,M}, \qquad \left\langle S_n^m, C_N^M \right\rangle_w = 0, \qquad \left\langle C_n^m, C_N^M \right\rangle_w = \gamma_{m,n}\delta_{n,N}\delta_{m,M}, \tag{4.16a}$$

where the normalization constants are given by

$$\gamma_{m,n} = \frac{2\pi(n+m)!}{(2n+1)(n-m)!} \times \begin{cases} 2, & m = 0; \\ 1, & m \neq 0. \end{cases} \tag{4.16b}$$

For the exterior problem requiring a finite solution as $\xi \to \infty$, the general solution of Laplace's equation with a source at coordinates (ξ_0, η_0, ϕ_0), is

$$G^e(\mathbf{x};\mathbf{x}_0) = \sum_{n=0}^{\infty}\sum_{m=0}^{n} B_{m,n} Q_n^m(\xi) P_n^m(\eta)\cos m(\phi-\phi_0), \tag{4.17}$$

with constants $B_{m,n}$. To apply the boundary condition, we note that the normal derivative on $\xi = \xi_0$ satisfies

$$\begin{aligned}\partial_n G^e &= \frac{a^2}{f} w(\xi_0,\eta)\partial_\xi G^e \\ &= \frac{a^2}{f} w(\xi_0,\eta)\sum_{n=0}^{\infty}\sum_{m=0}^{n} B_{m,n} Q_n^{m'}(\xi_0) P_n^m(\eta)\cos m(\phi-\phi_0) = -w(\xi_0,\eta)\delta(\eta-\eta_0)\delta(\phi-\phi_0).\end{aligned}$$

Applying the identities (4.16), we have that

$$B_{m,n} = -\frac{f}{a^2}\frac{P_n^m(\eta_0)}{\gamma_{m,n} Q_n^{m'}(\xi_0)} = \frac{1}{f(1-\xi_0^2)}\frac{P_n^m(\eta_0)}{\gamma_{m,n} Q_n^{m'}(\xi_0)}.$$

We hence obtain the series solution

$$G^e(\mathbf{x};\mathbf{x}_0) = \frac{1}{f(1-\xi_0^2)}\sum_{n=0}^{\infty}\sum_{m=0}^{n}\frac{P_n^m(\eta_0)}{\gamma_{m,n} Q_n^{m'}(\xi_0)} Q_n^m(\xi) P_n^m(\eta)\cos m(\phi-\phi_0). \tag{4.18}$$

We now turn to the issue of extracting the singularity structure by considering the solution of $G^e(\mathbf{x};\mathbf{x}_0)$ on the ring $r_c = |\mathbf{x}-\mathbf{x}_0|$ in the tangent plane at $\mathbf{x}_0$ (see Fig. 2.1). On this ring, we have that

$$G^e(\mathbf{x};\mathbf{x}_0) = \frac{1}{2\pi r_c} - \frac{\mathcal{H}(\mathbf{x}_0)}{4\pi}\log r_c + \frac{\mathcal{Q}(\mathbf{x}_0)}{8\pi}\cos(2\varphi) + R^e(\mathbf{x};\mathbf{x}_0) + o(1), \quad \text{as} \quad \mathbf{x}\to\mathbf{x}_0, \tag{4.19}$$

were φ is an azimuthal measure in the tangent plane. To isolate $R^e(\mathbf{x}_0;\mathbf{x}_0)$, we calculate the average value of the function

$$W(\mathbf{x};\mathbf{x}_0) = G^e(\mathbf{x};\mathbf{x}_0) - \frac{1}{2\pi r_c} + \frac{\mathcal{H}(\mathbf{x}_0)}{4\pi}\log r_c,$$

along a ring of points in the tangent plane at $\mathbf{x}_0$. To improve the convergence properties of the series, the series representation of the leading monopole singularity is subtracted from the expansion. The relevant series for the monopole expansion [55] around a source $\mathbf{x}_0 = (\xi_0,\eta_0,\phi_0)$ is

$$\frac{1}{|\mathbf{x}-\mathbf{x}_0|} = \frac{1}{f}\sum_{n=0}^{\infty}\sum_{m=0}^{n} H_{m,n} P_n^m(\eta_0) P_n^m(\xi_0) Q_n^m(\xi) P_n^m(\eta)\cos m(\phi-\phi_0). \tag{4.20a}$$

The constants $H_{m,n}$ are given by

$$H_{m,n} = \varepsilon_m(-1)^m(2n+1)\left[\frac{(n-m)!}{(n+m)!}\right]^2, \qquad \varepsilon_m = \begin{cases} 1, & m=0; \\ 2, & m>0. \end{cases} \tag{4.20b}$$

Adding and subtracting a monopole from the solution (4.18) yields

$$\begin{aligned}G^e(\mathbf{x};\mathbf{x}_0) &= \frac{1}{2\pi|\mathbf{x}-\mathbf{x}_0|} - \frac{1}{2\pi|\mathbf{x}-\mathbf{x}_0|} + \sum_{n=0}^{\infty}\sum_{m=0}^{n} B_{m,n} Q_n^m(\xi) P_n^m(\eta)\cos m(\phi-\phi_0) \\ &= \frac{1}{2\pi|\mathbf{x}-\mathbf{x}_0|} + \sum_{n=0}^{\infty}\sum_{m=0}^{n}\left[B_{m,n} - \frac{H_{m,n} P_n^m(\eta_0) P_n^m(\xi_0)}{2\pi f}\right] Q_n^m(\xi) P_n^m(\eta)\cos m(\phi-\phi_0),\end{aligned}$$

The series for the function $W(\mathbf{x};\mathbf{x}_0)$ is now given by

$$W(\mathbf{x};\mathbf{x}_0) = \frac{\mathcal{H}(\mathbf{x}_0)}{4\pi}\log r_c + \sum_{n=0}^{\infty}\sum_{m=0}^{n}\left[B_{m,n} - \frac{H_{m,n} P_n^m(\eta_0) P_n^m(\xi_0)}{2\pi f}\right] Q_n^m(\xi) P_n^m(\eta)\cos m(\phi-\phi_0). \tag{4.21}$$

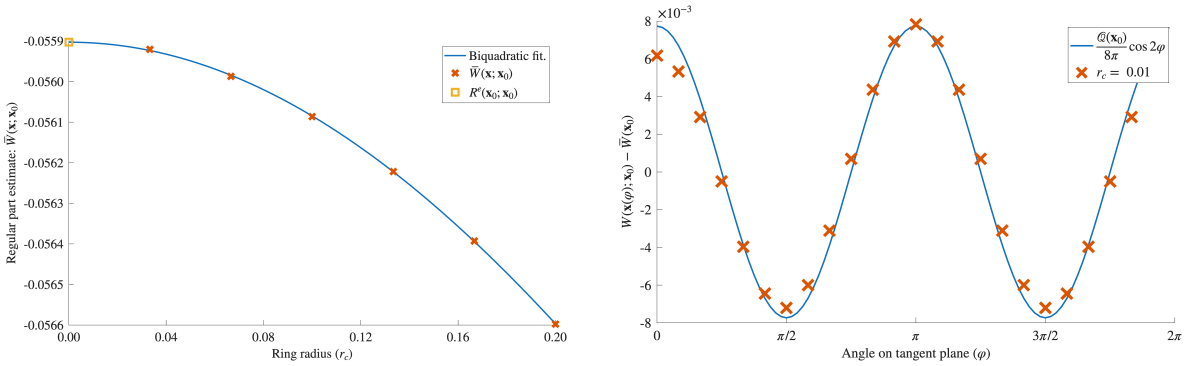

(a) $\bar{W}(\mathbf{x};\mathbf{x}_0)$ as $r_c \to 0$.

(b) $W(\mathbf{x};\mathbf{x}_0) - \bar{W}$ on the ring $r_c = |\mathbf{x} - \mathbf{x}_0| = 0.01$.

Fig. 4.3: Evaluation of the series $W(\mathbf{x};\mathbf{x}_0)$ on the tangent plane at $\eta_0 = 0.7$ with $N = 2000$ terms. Left: the approximation of the average $\bar{W}$ as the ring radius r_c shrinks to zero. We use a fitted curve (solid blue) to extrapolate the intercept as $R^e(\mathbf{x}_0;\mathbf{x}_0)$ (yellow square). Right: The quantity $W(\mathbf{x}(\varphi);\mathbf{x}_0) - \bar{W}$ at points (red squares) along a ring in the tangent plane centered at $\mathbf{x}_0$ together with the predicted asymptotic behavior (solid blue) in (4.19).

We evaluate $W(\mathbf{x};\mathbf{x}_0)$ on $N_{\text{ring}} = 24$ equally spaced points $\{\mathbf{x}_i\}_{i=1}^{N_{\text{ring}}}$ on a ring of radius r_c in the tangent plane. As $r_c \to 0$, we recover the predicted biquadratic (quadratic in r_c^2) behavior of $\bar{W} = \frac{1}{N_{\text{ring}}}\sum_{i=1}^{N_{\text{ring}}} W(\mathbf{x}_i;\mathbf{x}_0)$ and use fitting to extrapolate the value of $R^e(\mathbf{x}_0;\mathbf{x}_0)$ - see Fig. 4.3(a). Along the ring $|\mathbf{x} - \mathbf{x}_0| = r_c$, we directly verify in Fig. 4.3(b) the presence of the third weaker singularity predicted in (4.19). For the prolate spheroid, the mean and differences of the surface curvature at the point $\mathbf{x}_0$ are given by

$$\mathcal{H}(\mathbf{x}_0) = \frac{\xi_0(1 - 2\xi_0^2 + \eta_0^2)}{2f(\xi_0^2 - 1)^{\frac{1}{2}}(\xi_0^2 - \eta_0^2)^{\frac{3}{2}}}, \qquad \mathcal{Q}(\mathbf{x}_0) = \frac{\xi_0(1 - \eta_0^2)}{2f(\xi_0^2 - 1)^{\frac{1}{2}}(\xi_0^2 - \eta_0^2)^{\frac{3}{2}}}.$$

In our numerical evaluation of the series (4.21), we calculate only ratios and logarithmic derivatives of the Legendre functions P_n^m and Q_n^m rather than the functions themselves. This avoids evaluating the factorial terms in the normalization factors $\gamma_{m,n}$ which leads to overflow at relatively moderate n and m values in standard double precision. Recursion relations adapted for this purpose were provided in [54] which we have implemented and found to provide reliable evaluation for thousands of terms. Our results are based on evaluations of $W(\mathbf{x};\mathbf{x}_0)$ with truncation at 2000 terms.

In Fig. 4.4, we display comparisons of estimates of $R^e(\mathbf{x}_0;\mathbf{x}_0)$ from the series solution approach and the boundary integral method. We take a prolate spheroid with parameters $a = 1$, $b = \sqrt{2}$ and a source point at $\mathbf{x}_0 = (\xi_0, \eta_0, 0)$ for a range of points $\eta_0 \in [-1, 1]$ and $\xi_0 = b/\sqrt{b^2 - a^2} = \sqrt{2}$. We observe close agreement between the boundary integral method and the series solution. The relative error in the series approximation is around 10^{-4} which is limited by the number of terms in the truncation of the series and our extrapolation method. Consequently, the utility of this series solution is that it provides a non-trivial validation of both the numerical method and the derived singular behavior (4.19) of the Green's function near the source. As we demonstrated in Fig. 4.1, our numerical method is capable of relative errors of 10^{-12} for the bulk problem and 10^{-9} for the surface problem.

4.4. Applications to narrow capture problems. In this example, we demonstrate the ability of our method to inform on some open questions in narrow capture theory. For a bounded geometry $\Omega \subset \mathbb{R}^3$, the Narrow Capture Problem (NCP) [50, 13, 23] asks how should the locations $\{\mathbf{x}_i\}_{i=1}^N \in \Omega$ of N small well separated traps be arranged so as to minimize the average capture time τ of a diffusing molecule of diffusivity $D > 0$? For identical spherical traps of common radius ε, the quantity τ was shown to satisfy [14]

$$\tau \sim \frac{|\Omega|}{D}\left[\frac{1}{4\pi\varepsilon N} + \frac{p}{N^2}\right], \qquad p := p(\mathbf{x}_1, \ldots, \mathbf{x}_N) = \sum_{i=1}^{N}\left[R^i(\mathbf{x}_i;\mathbf{x}_i) + \sum_{\substack{j=1 \\ j\neq i}}^{N} G^i(\mathbf{x}_j;\mathbf{x}_i)\right], \tag{4.22}$$

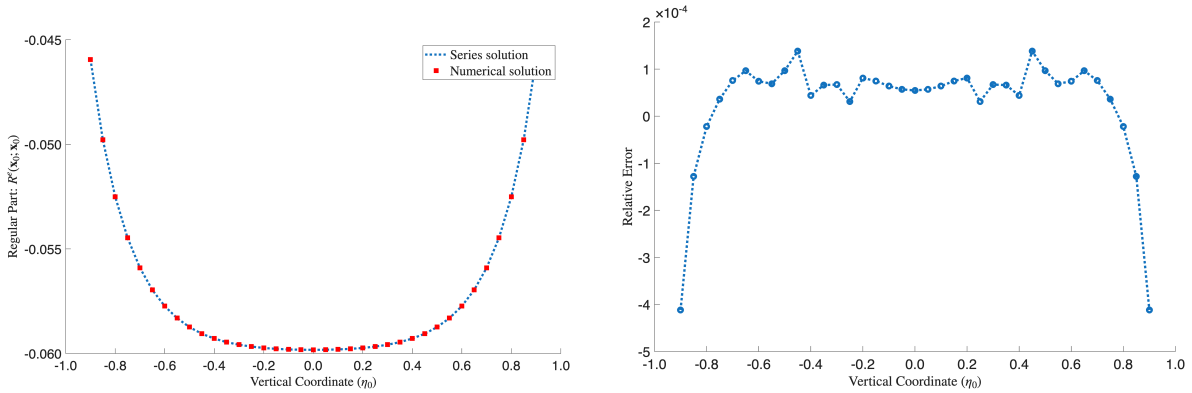

(a) Agreement in $R^e(\mathbf{x}_0;\mathbf{x}_0)$.

(b) Relative error in series approximation.

Fig. 4.4: Comparison between the regular part of the Green's function for the prolate spheroid case $a = 1$ and $b = \sqrt{2}$ for a range of source point in $\eta_0 \in [-1, 1]$. Left: A comparison of $R^e(\mathbf{x}_0;\mathbf{x}_0)$ from the series approximation (solid blue) and our numerical solution (red squares). Right: The relative error in the series approximation is roughly 10^{-4}.

as $\varepsilon \to 0$. The optimizing trap locations $\{\mathbf{x}_i\}_{i=1}^N$ therefore correspond to the minima of the discrete energy $p(\mathbf{x}_1, \ldots, \mathbf{x}_N)$. Minimization of similar discrete energies is a challenging computational problem on account of the multiplicity of critical points as N increases. A number of optimization strategies combine local (e.g. Newton methods) and global search methods (e.g. particle swarm optimization) [13, 23, 31]. In particular, it is essential to determine p and its gradient to high precision so that the optimization algorithm can discern between configurations that have close values in the objective function. The recent survey article [13] highlighted the lack of reliable methods to compute the Neumann function as a major obstacle towards progress on this problem.

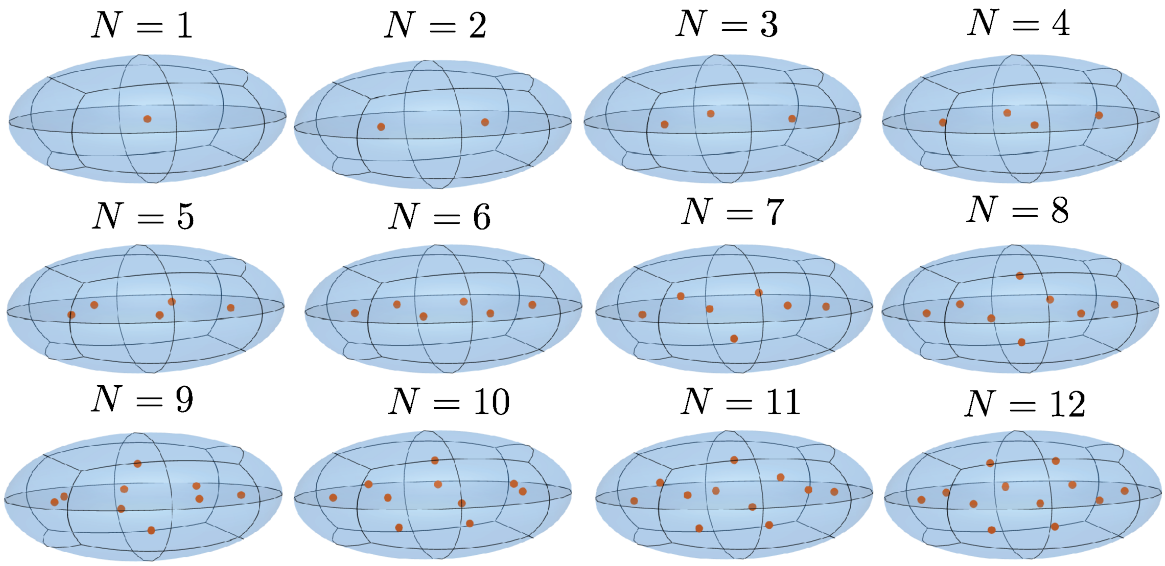

Fig. 4.5: Locally optimal trap configurations for $N = 1, \ldots, 12$ in the ellipsoid (4.23). For $1 \le N \le 6$, the optimizing configurations are coplanar on $z = 0$.

In this section we demonstrate the effectiveness of our method at predicting optimizing configurations when coupled with established optimization routines. We present results on minimizers of (4.22) obtained with the MATLAB optimization routine `fmincon` called with the `interior-point` algorithm. A notable aspect of our boundary integral method is that it provides a high precision calculation of the gradient of the objective function without the need for differencing.

The first example is a demonstration for the ellipsoidal domain

$$\frac{x^2}{a^2} + \frac{y^2}{b^2} + \frac{z^2}{c^2} = 1, \qquad (a, b, c) = \left(\frac{3}{2}, 1, \frac{2}{3}\right), \tag{4.23}$$

for $N = 1, \ldots, 12$ traps. We observe in Fig. 4.5 a geometric bifurcation where for $1 \leq N \leq 6$, the minimizing configurations are coplanar on $z = 0$ and not coplanar for $N \geq 7$. A similar bifurcation has been observed in the two dimensional case of an ellipse where the minimizing set transitions from colinearity [31, 9, 13].

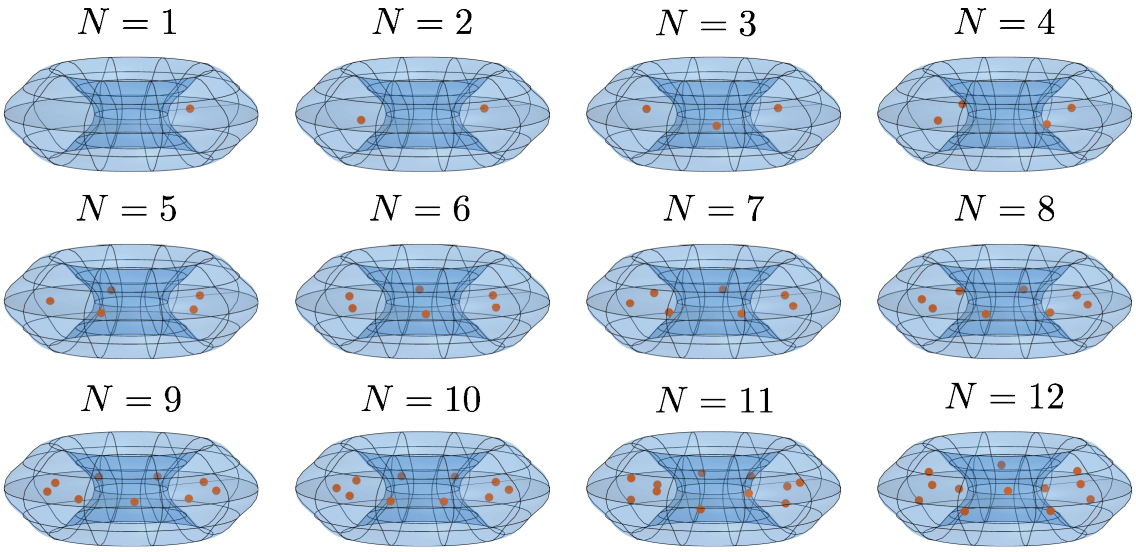

Fig. 4.6: Minimizing locations of (4.22) for $N = 1, \ldots, 12$ trap locations (red dots) in the torus defined in equation (4.24). For $1 \leq N \leq 10$, the optimizing configuration is coplanar with $z = 0$.

In a second example, we compute some minimizing configurations for the toroidal domain specified by

$$x(\theta, \phi) = \left(r_{\text{maj}} + \cos\theta \left(r_{\text{min}} + r_{\text{wave}} \cos n\theta\right)\right) \cos\phi, \tag{4.24a}$$

$$y(\theta, \phi) = \left(r_{\text{maj}} + \cos\theta \left(r_{\text{min}} + r_{\text{wave}} \cos n\theta\right)\right) \sin\phi, \tag{4.24b}$$

$$z(\theta, \phi) = \left(r_{\text{min}} + r_{\text{wave}} \cos n\theta\right) \sin\theta, \tag{4.24c}$$

for $(\theta, \phi) \in (0, 2\pi]^2$. We take the parameter values

$$(r_{\text{maj}}, r_{\text{min}}, r_{\text{wave}}, n) = (1, 0.5, 0.05, 4),$$

which represents a toroidal geometry with cross-sectional profile given by a near-circular disk. For the toroidal domain, we see in Fig. 4.6 that for configurations $1 \leq N \leq 10$, the optimizing configuration is coplanar with $z = 0$ while for $N \geq 11$, the minimizing configuration undergoes a geometric bifurcation into the region $z \neq 0$.

For both the ellipsoid and toroidal geometries, we show in Fig. 4.7 the calculated minimum energy p as a function of N for $N = 1, \ldots, 12$ trap configurations. The calculated minimum energy p as a function of N and again observe a function that decreases smoothly through this transition.

For a general domain Ω, it would be desirable to derive an explicit formula for the minimizer of p in the limit as $N \to \infty$ which can be verified with this method. This question relates to problems in Coulomb gases [48] and also appears in the concentration sets of nonlinear PDEs in singularly perturbed limits [10, 18, 19, 33, 51]. Interestingly, despite the bifurcation from planar (red dots) to non-planar (yellow dots) trap configurations, the curve of minimizing energy appears to be smooth through this transition.

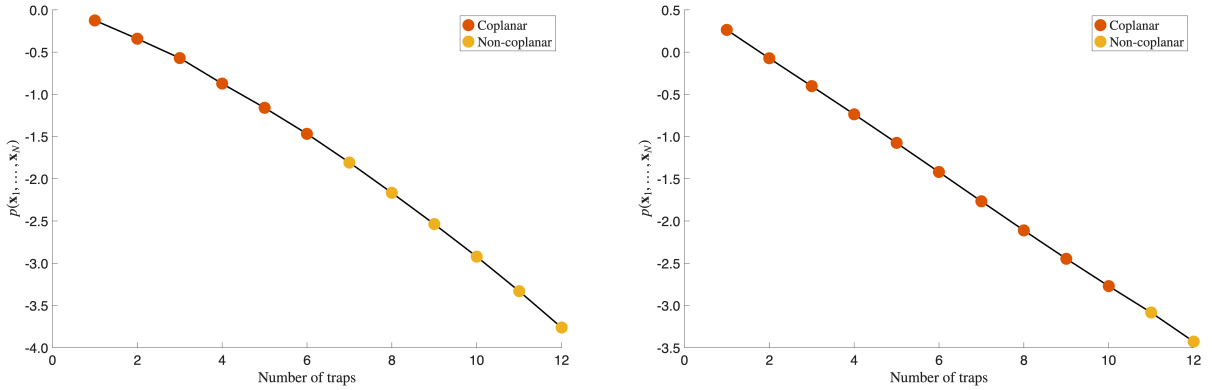

(a) Energy scaling for the ellipsoid domain.

(b) Energy scaling for the toroidal domain.

Fig. 4.7: Minimizing values of the discrete energy (4.22) for $N = 1, \ldots, 12$ for the ellipsoidal (left) domain (4.23) and the toroidal (right) domain (4.24). The geometric bifurcation from planar (red dots) to non planar (yellow dots) optimizing configurations occurs at $N \geq 7$ for the ellipsoid and $N \geq 11$ for the torus.

4.5. The regular part on some general geometries. In this final section, we present results of our method for the computation of the interior $R^i(\mathbf{x};\mathbf{x})$ and exterior $R^e(\mathbf{x};\mathbf{x})$ surface regular parts for $\mathbf{x} \in \partial\Omega$ which are key to addressing the narrow escape problem. The study of [43] determined that the quantity $R^i(\mathbf{x};\mathbf{x})$ describes how the location $\mathbf{x} \in \partial\Omega$ of a boundary window modulates the expected exit time of diffusing particles from an enclosed geometry. In particular, lower values of $R^i(\mathbf{x};\mathbf{x})$ are associated with faster escape times. We remark that the study [43] adopted the normalization condition $\int_{\partial\Omega} G^i(\mathbf{x};\mathbf{y})\mathrm{d}A(\mathbf{x}) = 0$ which will modulate the value of $R^i(\mathbf{x};\mathbf{x})$ while retaining the singularity structure (1.3). To demonstrate the potential of this method for the determination of optimizing locations of boundary windows, we calculate these quantities for three geometries.

The biconcave disk, which approximates the geometry of blood-cells [46], is given by the surface

$$x(\theta,\phi) = \alpha \sin\theta\cos\phi, \qquad y(\theta,\phi) = \alpha\sin\theta\sin\phi \qquad z(\theta,\phi) = \frac{\alpha}{2}\left(b + c\sin^2\theta - d\sin^4\theta\right)\cos\theta, \tag{4.25a}$$

where $\phi \in [0, 2\pi)$ and $\theta \in [0, \pi)$. The shape parameters are given by [46]

$$\alpha = 1.38581994, \qquad b = 0.207, \qquad c = 2.003, \qquad d = 1.123. \tag{4.25b}$$

In Fig. 4.8, we plot solutions of the interior ($R^i(\mathbf{x};\mathbf{x})$) and exterior ($R^e(\mathbf{x};\mathbf{x})$) surface regular parts for the geometry (4.25). In the case of the prolate spheroid with principal semi-axes $(a, b, c) = (1, 1, \sqrt{2})$, we show in Fig. 4.9 the numerical solution of $R^i(\mathbf{x};\mathbf{x})$ and $R^e(\mathbf{x};\mathbf{x})$ on the surface. Finally, in Fig. 4.10 we plot the regular parts for a surface given by the unit sphere perturbed by a spherical harmonic, $0.3 \cdot \Re Y_6^4$. This surface has been used to model non-spherical perturbations of real cells [1, 7].

In the case of the blood cell shaped domain, we see in Fig. 4.8(a) that the lowest value of $R^i(\mathbf{x};\mathbf{x})$ is attained at the dimple where the surface curvature is at a critical point. A similar optimizing preference was observed in [9] for the planar case. In Fig. 4.9(a) we see that the lowest value of $R^i(\mathbf{x};\mathbf{x})$ is attained on the equator. We remark that at the poles and the equator, the mean curvatures are

$$\mathcal{H}_{\text{pole}} = -\frac{c}{a^2} = -\sqrt{2}, \qquad \mathcal{H}_{\text{eq}} = -\frac{c^2 + a^2}{2ac^2} = -\frac{3}{4},$$

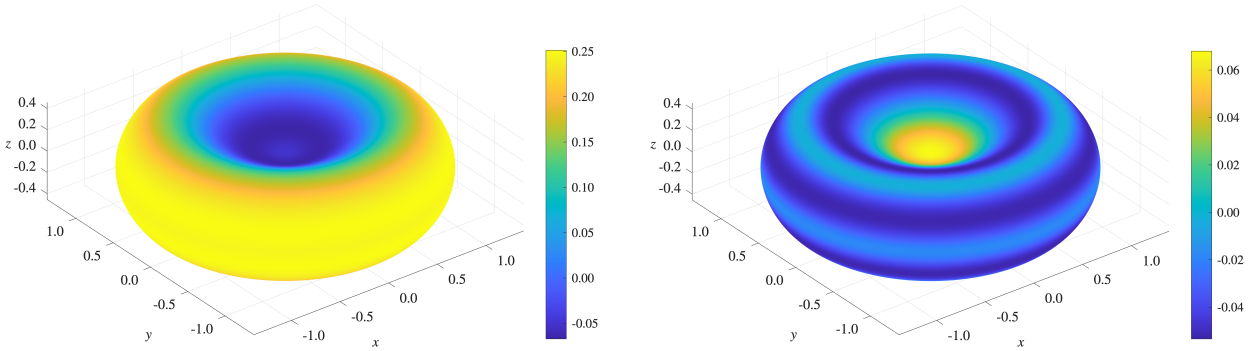

(a) $R^i(\mathbf{x};\mathbf{x})$ for $\mathbf{x} \in \partial\Omega$. (b) $R^e(\mathbf{x};\mathbf{x})$ for $\mathbf{x} \in \partial\Omega$.

Fig. 4.8: Numerically computed values of the interior (left) and exterior (right) regular parts for the blood cell shape domain (4.25).

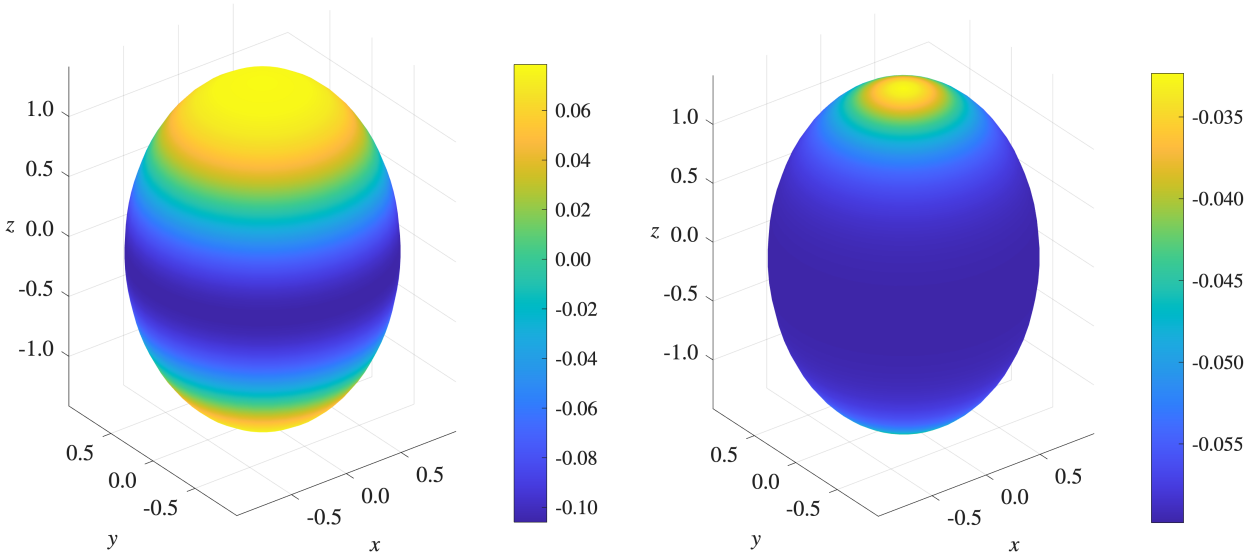

(a) $R^i(\mathbf{x};\mathbf{x})$ for $\mathbf{x} \in \partial\Omega$. (b) $R^e(\mathbf{x};\mathbf{x})$ for $\mathbf{x} \in \partial\Omega$.

Fig. 4.9: Numerically computed values of the interior (left) and exterior (right) regular parts of the Neumann function on a prolate spheroid with principal semi-axes $(a, b, c) = (1, 1, \sqrt{2})$.

so that $\mathcal{H}_{\text{eq}} > \mathcal{H}_{\text{pole}}$. We observe a simple correspondence between the maximum and minimum values of $R^i(\mathbf{x};\mathbf{x})$ and $\mathcal{H}(\mathbf{x})$ for $\mathbf{x} \in \partial\Omega$ in the case of a prolate spheroid. Specifically, the value of $R(\mathbf{x};\mathbf{x})$ is minimized at the equator of the prolate spheroid - a point at which the curvature is maximized. For arbitrary geometries, we expect that $R(\mathbf{x};\mathbf{x})$ will depend on both local and global geometric features in a non-trivial way. It remains an open problem to describe the minimizing set of boundary windows for a general geometry, however, the numerical tool developed here can provide highly accurate estimates of the key quantities involved in this optimization problem.

5. Discussion. In this paper we have considered the three dimensional Neumann Green's function and provided numerical methodologies to evaluate this quantity for general geometries. In the particular case of a surface source located on a curved geometry, we derived a three term expansion for the singularity structure that depends on local geometric features through the sum and difference of the principal curvatures. With this explicit information, we implemented a high order boundary integral method to recover the remaining

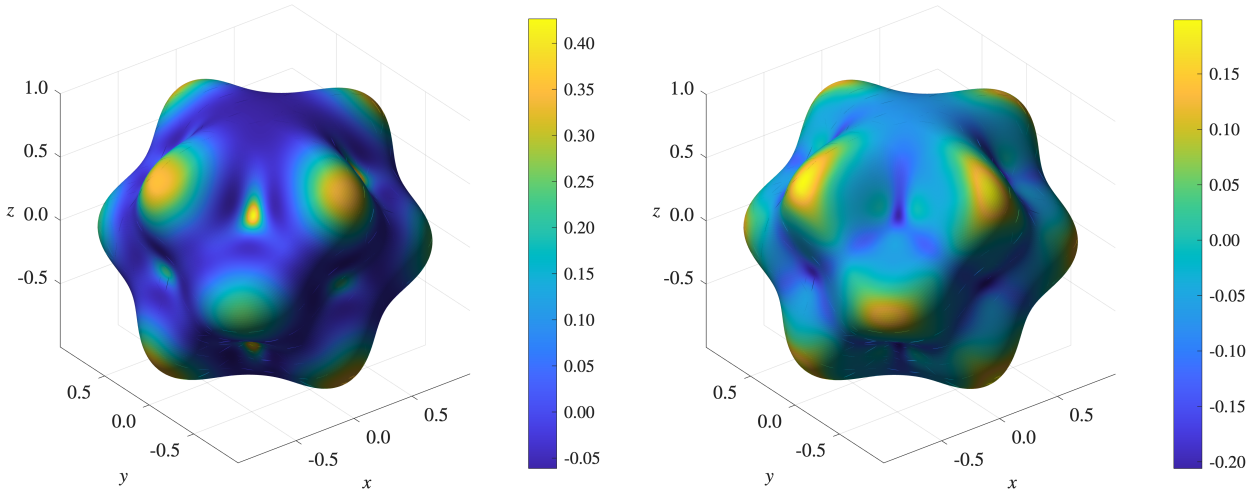

(a) $R^i(\mathbf{x};\mathbf{x})$ for $\mathbf{x} \in \partial\Omega$.

(b) $R^e(\mathbf{x};\mathbf{x})$ for $\mathbf{x} \in \partial\Omega$.

Fig. 4.10: Numerically computed values of the interior (left) and exterior (right) regular parts of the Neumann function on a sphere that has been perturbed by Y_6^4.

regular part of the Green's function. For problems posed either interior or exterior to Ω, with a bulk or surface source, we provide a high-order numerical routine to evaluate the Green's function, its regular part and their gradients. The method was validated on a number of test cases including the sphere, prolate spheroid and a family of constructed geometries.

As an application of our method to an open problem in diffusion theory, we computed optimizing trap configurations for the narrow capture problem in ellipsoid and toroidal domains. We observed a geometric bifurcation where the optimal placement transitions away from a co-planar structure as N increases. We anticipate that this numerical method will be a useful tool in studying related problems in capture theory, particularly in the open problem of determining the optimal configurations of boundary traps and identifying the limiting configurations as $N \to \infty$.

Singular perturbation methods are a powerful tool for studying problems with strongly localized phenomena, such as spot dynamics in reaction-diffusion systems or narrow escape in diffusion theory [51, 43, 6]. In these settings the localized dynamics are globally coupled through the appropriate Neumann Green's function, and for sites localized on the boundary the influence of surface geometry is encoded in the diagonal regular part $R^{i,e}(\mathbf{x};\mathbf{x})$ for $\mathbf{x} \in \partial\Omega$. In Section 4.5 we computed this quantity across several representative geometries, demonstrating that the method resolves the geometric dependence relevant to surface-mediated reaction dynamics. The high-order approaches developed here can therefore broaden the range of geometries in which singular perturbation techniques are tractable.

An important avenue for extension of this work is to other operators such as the modified Helmholtz operator which arises when the Laplace transform is applied to the heat equation. This approach is one route [36, 4, 11, 12, 38, 16] to reproduce the time-dependent statistics [25] of the dynamics arrival rate at reactive sites. These quantities are essential to determine extreme statistics for first passage time problems [39, 41].

Acknowledgments. AEL acknowledges support from the NSF under grant DMS-2052636. JGH was supported in part by a Sloan Research Fellowship. TG was supported by an AMS-Simons Travel Grant. This research was supported in part by grants from the NSF (DMS-2235451) and Simons Foundation (MPS-NITMB-00005320) to the NSF-Simons National Institute for Theory and Mathematics in Biology (NITMB).

REFERENCES

[1] A. Alonso, R. G. Endres, and J. B. Kirkegaard, *Local clustering and global spreading of receptors for optimal spatial*

gradient sensing, Phys. Rev. Lett., 134 (2025), p. 158401, doi:10.1103/PhysRevLett.134.158401, https://link.aps.org/doi/10.1103/PhysRevLett.134.158401.

[2] T. Askham, L. Greengard, J. Hoskins, L. Lu, M. O'Neil, M. Rachh, F. Vico, and V. Rokhlin, *fmm3dbie: FMM-accelerated boundary integral equation solvers*, https://github.com/fastalgorithms/fmm3dbie.

[3] S. Bergman and M. Schiffer, *Kernel Functions and Elliptic Differential Equations in Mathematical Physics*, vol. 4 of Pure and Applied Mathematics, Academic Press, New York, 1953.

[4] A. J. Bernoff and A. E. Lindsay, *Kinetic Monte Carlo methods for three-dimensional diffusive capture problems in exterior domains*, Royal Society Open Science, 12 (2025), p. 241033, doi:10.1098/rsos.241033, https://royalsocietypublishing.org/doi/abs/10.1098/rsos.241033, arXiv:https://royalsocietypublishing.org/doi/pdf/10.1098/rsos.241033.

[5] J. Bremer and Z. Gimbutas, *On the numerical evaluation of the singular integrals of scattering theory*, Journal of Computational Physics, 251 (2013), pp. 327–343, doi:https://doi.org/10.1016/j.jcp.2013.05.048, https://www.sciencedirect.com/science/article/pii/S0021999113004166.

[6] P. C. Bressloff, *Cellular diffusion processes in singularly perturbed domains*, Journal of Mathematical Biology, 89 (2024), p. 58.

[7] H. Cavanagh, D. Kempe, J. K. Mazalo, M. Biro, and R. G. Endres, *T cell morphodynamics reveal periodic shape oscillations in three-dimensional migration*, Journal of The Royal Society Interface, 19 (2022), p. 20220081.

[8] S. Chaillat, B. Cotté, J.-F. Mercier, G. Serre, and N. Trafny, *Efficient evaluation of three-dimensional helmholtz green's functions tailored to arbitrary rigid geometries for flow noise simulations*, Journal of Computational Physics, 452 (2022), p. 110915, doi:https://doi.org/10.1016/j.jcp.2021.110915, https://www.sciencedirect.com/science/article/pii/S002199912100810X.

[9] S. Chakraborty, J. Hoskins, and A. E. Lindsay, *Fast integral methods for the neumann green's function: applications to capture and signaling problems in two dimensions*, 2025, https://arxiv.org/abs/2511.08458, arXiv:2511.08458.

[10] W. Chen and M. J. Ward, *The stability and dynamics of localized spot patterns in the two-dimensional gray–scott model*, SIAM Journal on Applied Dynamical Systems, 10 (2011), pp. 582–666, doi:10.1137/09077357X.

[11] J. Cherry, A. E. Lindsay, A. Navarro Hernández, and B. Quaife, *Trapping of Planar Brownian Motion: Full First Passage Time Distributions by Kinetic Monte Carlo, Asymptotic, and Boundary Integral Methods*, Multiscale Modeling & Simulation, 20 (2022), pp. 1284–1314, doi:10.1137/21M146380X.

[12] J. Cherry, A. E. Lindsay, and B. D. Quaife, *Boundary integral methods for particle diffusion in complex geometries: Shielding, confinement, and escape*, Journal of Computational Physics, 534 (2025), p. 114032, doi:https://doi.org/10.1016/j.jcp.2025.114032, https://www.sciencedirect.com/science/article/pii/S0021999125003158.

[13] A. Cheviakov and M. Ward, *Optimization of Trap Locations for Narrow Capture Problems*, Springer Nature Switzerland, Cham, 2024, pp. 225–246.

[14] A. Cheviakov and M. J. Ward, *Optimizing the principal eigenvalue of the Laplacian in a sphere with interior traps*, Math. and Comp. Model., 53 (2011), pp. 1394–1409.

[15] A. F. Cheviakov, M. J. Ward, and R. Straube, *An asymptotic analysis of the mean first passage time for narrow escape problems: Part ii: The sphere*, Multiscale Modeling & Simulation, 8 (2010), pp. 836–870.

[16] H. L. Croix and A. E. Lindsay, *The lightning method for the heat equation*, Journal of Scientific Computing, 107 (2026).

[17] G. Dassios and J. C.-E. Sten, *On the neumann function and the method of images in spherical and ellipsoidal geometry*, Mathematical Methods in the Applied Sciences, 35 (2012), pp. 482–496, doi:https://doi.org/10.1002/mma.1595, https://onlinelibrary.wiley.com/doi/abs/10.1002/mma.1595, arXiv:https://onlinelibrary.wiley.com/doi/pdf/10.1002/mma.1595.

[18] J. Dávila and J. Wei, *Point ruptures for a mems equation with fringing field*, Communications in Partial Differential Equations, 37 (2012), pp. 1462–1493, doi:10.1080/03605302.2012.679990, https://doi.org/10.1080/03605302.2012.679990.

[19] M. del Pino, M. Kowalczyk, and M. Musso, *Singular limits in liouville-type equations*, Calculus of Variations and Partial Differential Equations, 24 (2005), pp. 47–81.

[20] M. G. Duffy, *Quadrature over a pyramid or cube of integrands with a singularity at a vertex*, SIAM journal on Numerical Analysis, 19 (1982), pp. 1260–1262.

[21] P. R. Garabedian, *Partial Differential Equations*, John Wiley & Sons, New York, 1964.

[22] C. Geuzaine and J.-F. Remacle, *Gmsh: A 3-d finite element mesh generator with built-in pre- and post-processing facilities*, International Journal for Numerical Methods in Engineering, 79 (2009), pp. 1309–1331, doi:https://doi.org/10.1002/nme.2579, https://onlinelibrary.wiley.com/doi/abs/10.1002/nme.2579, arXiv:https://onlinelibrary.wiley.com/doi/pdf/10.1002/nme.2579.

[23] J. Gilbert and A. Cheviakov, *Global optimisation of the mean first passage time for narrow capture problems in elliptic domains*, European Journal of Applied Mathematics, 34 (2023), p. 1269–1287, doi:10.1017/S0956792522000341.

[24] D. Gomez and A. F. Cheviakov, *Asymptotic analysis of narrow escape problems in nonspherical three-dimensional domains.*, Phys Rev E Stat Nonlin Soft Matter Phys, 91 (2015), p. 012137.

[25] D. S. Grebenkov, R. Metzler, and G. Oshanin, *Full distribution of first exit times in the narrow escape problem*, New Journal of Physics, 21 (2019), p. 122001, doi:10.1088/1367-2630/ab5de4, https://doi.org/10.1088/1367-2630/ab5de4.

[26] D. S. Grebenkov and M. J. Ward, *The effective reactivity for capturing brownian motion by partially reactive patches on a spherical surface*, Multiscale Modeling & Simulation, 24 (2026), pp. 660–692, doi:10.1137/25M180562X.

[27] L. Greengard, M. O'Neil, M. Rachh, and F. Vico, *Fast multipole methods for the evaluation of layer potentials with locally-corrected quadratures*, Journal of Computational Physics: X, 10 (2021), p. 100092, doi:https://doi.org/10.1016/j.jcpx.2021.100092, https://www.sciencedirect.com/science/article/pii/S2590055221000093.

[28] L. Greengard and V. Rokhlin, *A fast algorithm for particle simulations*, Journal of computational physics, 73 (1987),

pp. 325–348.
[29] K. L. Ho and L. Greengard, *A fast direct solver for structured linear systems by recursive skeletonization*, SIAM Journal on Scientific Computing, 34 (2012), pp. A2507–A2532.
[30] G. C. Hsiao and W. L. Wendland, *Boundary integral equations*, in Boundary Integral Equations, Springer, 2021, pp. 25–94.
[31] S. A. Iyaniwura, T. Wong, C. B. Macdonald, and M. J. Ward, *Optimization of the mean first passage time in near-disk and elliptical domains in 2-d with small absorbing traps*, SIAM Review, 63 (2021), pp. 525–555.
[32] K. Kaiyrbekov and B. A. Camley, *Does nematic order allow groups of elongated cells to sense electric fields better?*, PLOS ONE, 20 (2025), pp. 1–20, doi:10.1371/journal.pone.0325800, https://doi.org/10.1371/journal.pone.0325800.
[33] T. Kolokolnikov, M. Ward, and J. Wei, *Spot self-replication and dynamics for the schnakenburg model*, J. Nonlinear Science, 19 (2009), pp. 302–332.
[34] R. Kress, *Linear Integral Equations*, Applied Mathematical Sciences, Springer, 2014, doi:10.1007/978-1-4612-0559-3.
[35] S. D. Lawley, A. E. Lindsay, and C. E. Miles, *Receptor organization determines the limits of single-cell source location detection.*, Phys Rev Lett, 125 (2020), p. 018102.
[36] A. E. Lindsay, A. J. Bernoff, and A. Navarro Hernández, *Short-time diffusive fluxes over membrane receptors yields the direction of a signalling source*, Royal Society Open Science, 10 (2023), p. 221619, doi:10.1098/rsos.221619, https://royalsocietypublishing.org/doi/abs/10.1098/rsos.221619, arXiv:https://royalsocietypublishing.org/doi/pdf/10.1098/rsos.221619.
[37] A. E. Lindsay, A. J. Bernoff, and M. J. Ward, *First passage statistics for the capture of a brownian particle by a structured spherical target with multiple surface traps*, Multiscale Modeling & Simulation, 15 (2017), pp. 74–109.
[38] A. E. Lindsay, R. T. Spoonmore, and J. C. Tzou, *Hybrid asymptotic-numerical approach for estimating first-passage-time densities of the two-dimensional narrow capture problem*, Phys. Rev. E, 94 (2016), p. 042418, doi:10.1103/PhysRevE.94.042418, https://link.aps.org/doi/10.1103/PhysRevE.94.042418.
[39] S. Linn and S. D. Lawley, *Extreme hitting probabilities for diffusion**, Journal of Physics A: Mathematical and Theoretical, 55 (2022), p. 345002, doi:10.1088/1751-8121/ac8191, https://doi.org/10.1088/1751-8121/ac8191.
[40] P.-G. Martinsson and M. O'Neil, *Fast direct solvers*, arXiv preprint arXiv:2511.07773, (2025).
[41] J. Morgan and A. Lindsay, *Modulation of antigen discrimination by duration of immune contacts in a kinetic proofreading model of T cell activation with extreme statistics*, PLOS Comp. Biol., 19 (2023), pp. 1–17.
[42] I. M. Nemenman and A. S. Silbergleit, *Explicit Green's function of a boundary value problem for a sphere and trapped flux analysis in Gravity Probe B experiment*, J. Appl. Phys., 86 (1999), pp. 614–624.
[43] M. Nursultanov, J. C. Tzou, and L. Tzou, *On the mean first arrival time of brownian particles on riemannian manifolds*, Journal de Mathématiques Pures et Appliquées, 150 (2021), pp. 202–240, doi:https://doi.org/10.1016/j.matpur.2021.04.006, https://www.sciencedirect.com/science/article/pii/S0021782421000611.
[44] P.-O. Persson and G. Strang, *A simple mesh generator in MATLAB*, SIAM Review, 46 (2004), pp. 329–345, doi:10.1137/S0036144503429121.
[45] C. E. Plunkett and S. D. Lawley, *Boundary homogenization for partially reactive patches*, Multiscale Modeling & Simulation, 22 (2024), pp. 784–810, doi:10.1137/23M1573422.
[46] C. Pozrikidis, *Numerical simulation of the flow-induced deformation of red blood cells*, Annals of Biomedical Engineering, 31 (2003), pp. 1194–1205.
[47] B. Schamberger, A. Roschger, R. Ziege, K. Anselme, M. B. Amar, M. Bykowski, A. P. G. Castro, A. Cipitria, R. Coles, R. Dimova, M. Eder, S. Ehrig, L. M. Escudero, M. E. Evans, P. R. Fernandes, P. Fratzl, L. Geris, N. Gierlinger, E. Hannezo, A. Iglič, J. J. K. Kirkensgaard, P. Kollmannsberger, Ł. Kowalewska, N. A. Kurniawan, I. Papantoniou, L. Pieuchot, T. H. V. Pires, L. Renner, A. Sageman-Furnas, G. E. Schröder-Turk, A. Sengupta, V. R. Sharma, A. Tagua, C. Tomba, X. Trepat, S. L. Waters, E. Yeo, C. M. Bidan, and J. W. C. Dunlop, *Curvature in biological systems: Its quantification, emergence, and implications across the scales*, Advanced Materials, 35 (2023), p. 2206110, doi:https://doi.org/10.1002/adma.202206110, https://advanced.onlinelibrary.wiley.com/doi/abs/10.1002/adma.202206110, arXiv:https://advanced.onlinelibrary.wiley.com/doi/pdf/10.1002/adma.202206110.
[48] S. Serfaty, *Lectures on coulomb and riesz gases*, 2024, https://arxiv.org/abs/2407.21194, arXiv:2407.21194.
[49] A. Silbergleit, I. Mandel, and I. Nemenman, *Potential and field singularity at a surface point charge*, Journal of Mathematical Physics, 44 (2003), pp. 4460–4466.
[50] A. Singer, Z. Schuss, D. Holcman, and R. S. Eisenberg, *Narrow escape, part i*, Journal of Statistical Physics, 122 (2006), pp. 437–463.
[51] J. C. Tzou, S. Xie, T. Kolokolnikov, and M. J. Ward, *The stability and slow dynamics of localized spot patterns for the 3-d schnakenberg reaction-diffusion model*, SIAM Journal on Applied Dynamical Systems, 16 (2017), pp. 294–336.
[52] B. Vioreanu and V. Rokhlin, *Spectra of multiplication operators as a numerical tool*, SIAM Journal on Scientific Computing, 36 (2014), pp. A267–A288.
[53] H. Xiao and Z. Gimbutas, *A numerical algorithm for the construction of efficient quadrature rules in two and higher dimensions*, Computers & mathematics with applications, 59 (2010), pp. 663–676.
[54] C. Xue and S. Deng, *Recursive computation of logarithmic derivatives, ratios, and products of spheroidal harmonics and modified bessel functions and applications*, Journal of Scientific Computing, 75 (2018), pp. 128–156.
[55] C. Xue, R. Edmiston, and S. Deng, *Image theory for neumann functions in the prolate spheroidal geometry*, Advances in Mathematical Physics, 2018 (2018), p. 7683929, doi:https://doi.org/10.1155/2018/7683929, https://onlinelibrary.wiley.com/doi/abs/10.1155/2018/7683929, arXiv:https://onlinelibrary.wiley.com/doi/pdf/10.1155/2018/7683929.